PETROPHYSICS, VOL. 64, NO. 5 (OCTOBER 2023); PAGES 656–679; 9 FIGURES, 1 TABLE. DOI: 10.30632/PJV64N5-2023a4

Flow-Dependent Relative Permeability Scaling for Steady-State Two-Phase Flow in Porous Media: Laboratory Validation on a Microfluidic Network

Nikolaos Karadimitriou[1], Marios S. Valavanides[2,*], Konstantinos Mouravas[2], and Holger Steeb[1]

ABSTRACT

Conventionally, the relative permeabilities of two immiscible fluid phases flowing in porous media are considered and expressed as functions of saturation. Yet, this has been put into challenge by theoretical, numerical, and laboratory studies of flow in artificial pore network models and real porous media. These works have revealed a significant dependency of the relative permeabilities on the flow rates, especially when the flow regime is capillary to capillary-viscous dominated, and part of the disconnected nonwetting phase remains mobile. These studies suggest that relative permeability models should include the functional dependence on flow intensities. However, revealing the explicit form of such dependence remains a persistent problem. Just recently, a general form of dependence was inferred based on extensive simulations with the DeProF model for steady-state two-phase flows in pore networks. The simulations revealed a systematic dependence of the relative permeabilities on the local flow rate intensities. This dependence can be described analytically by a universal scaling functional form of the actual independent variables of the process, namely, the capillary number, *Ca*, and the flow rate ratio, *r*. The proposed scaling incorporated a kernel function, the intrinsic dynamic capillary pressure (IDCP) function, describing the transition between capillarity- and viscosity-dominated flow phenomena. In a parallel laboratory study, SCAL measurements provided a preliminary proof-of-concept on the applicability of the model.

In the laboratory study presented here, we examine the applicability of the scaling model by taking extensive, ex-core measurements of relative permeabilities for steady-state co-injections of two immiscible fluids within an artificial microfluidic pore network, across different flow regimes in *Ca* and *r*.

From these measurements, we calculate the values of the mobility ratio, and we compare these to the corresponding values of the flow rate ratio. We also extract the IDCP curve, the locus of critical flow conditions, whereby the process is more efficient in terms of energy utilization – accounted by the nonwetting phase flow rate per unit of total power provided to the process, as well as the locus of flow conditions of equal relative permeabilities. We show that the degree of consistency between flow rate ratio and mobility ratio values, the IDCP curve, the locus of critical flow conditions, and the locus of equal relative permeabilities, as well as some associated invariant characteristic values, can be used for assessing the extent of end effects and for characterizing the flow as capillary- or viscous-dominated.

The proposed scaling introduces new opportunities for enhancing SCAL protocols and their associated applications. These include the characterization of systems and flow conditions, dynamic rock typing, evaluation of capillary end effects, as well as the advancement of more efficient field-scale simulators. Additionally, it paves the way in designing more energy-efficient EOR interventions.

INTRODUCTION

The conventional use of saturation as the independent variable in two-phase flow in porous media (PM) is based on the oversimplifying assumption that disconnected fluidic elements of the nonwetting phase (NWP), i.e., ganglia and droplets, do not move with the average flow but remain stranded in the porous medium matrix. Nevertheless, there is ample experimental evidence that disconnected, intermittent flow is a substantial and sometimes prevailing flow pattern (Tsakiroglou et al., 2007; Tallakstad et al., 2009; Guillen et al., 2012; Georgiadis et al., 2013; Aursjø et al., 2014; Datta et al., 2014; Oughanem et al., 2015; Armstrong et al., 2016).

Flow conditions have an adverse effect on the momentum balance and, in particular, on the relevant magnitude of the Stokes flow resistances, due to the bulk viscosity of the

Manuscript received by the Editor March 1, 2023; revised manuscript received August 21, 2023; manuscript accepted August 26, 2023.
[1]Institute of Applied Mechanics, University of Stuttgart, Germany, nikos.karadimitriou@mechbau.uni-stuttgart.de; holger.steeb@mechbau.uni-stuttgart.de
[2]Dept. of Civil Engineering, University of West Attica, Greece, marval@uniwa.gr; civ18394172@uniwa.gr
[*]Corresponding author, marval@uniwa.gr

NWP and the wetting phase (WP), and the Young-Laplace resistances, due to the contact line forces between the NWP/WP menisci and the pore walls. The former depends on local (microscale/pore scale) velocity gradients, in contrast to the latter, which are relatively independent of the displacement rates of the menisci. From an energy point of view, the power dissipation, due to bulk viscosity, scales with the square of the local velocity gradients, whereas the capillarity-induced dissipation scales with the rates of displacement of the menisci. For relatively low values of the superficial velocity, viscosity effects are insignificant compared to capillarity effects; as flow intensity is progressively increased, viscosity takes over from capillarity, and the flow progressively mutates from capillarity-dominated to transient capillary-viscosity- to viscosity-dominated flow (Valavanides, 2018b).

Treating relative permeabilities as functions of the saturation has been shown to be inefficient in providing a correct and specific enough description of the process across the domain of all possible flow conditions, as extensively discussed by Valavanides (2018b). A particular value in saturation does not necessarily imply that a unique disconnected structure of the NWP will settle in. Disconnected structures of the NWP can be coarsely described by a spectrum of population density distributions, extending from distributions of "many and small" fluidic elements, e.g., droplets and small ganglia, to "fewer and larger" fluidic elements, e.g., small and large ganglia. For any one of those cases, the corresponding superficial velocity of the disconnected NWP would not necessarily attain the same value. The latter would be the result of the antagonism between the two factors inhibiting the transport of each phase, i.e., viscosity and capillarity, over the mass and momentum balances. As a consequence, for any two different cluster configurations, i.e., any two different population density size distributions of disconnected phase, the effective permeabilities of the WP and the NWP would differ. Yet, those different cluster configurations and different values of the relative permeabilities could—in general—correspond to the same saturation value. In such situations, a universal, saturation-dependent description of the flow would be weak.

In addition, during core analysis, saturation is measured indirectly and cannot be externally imposed directly; it is only through control of a combination of pressure difference and/or flow rate of the NWP or the WP that the system will attain an average saturation. If one wants to consistently and systematically describe the process in the entire flow regime, extending across the broadest possible domain of the capillary number and the viscosity ratio, one has to consider those variables that describe the externally imposed conditions and contain macroscopic kinematic information. The phase superficial velocities or, equivalently, the capillary number and the flow rate ratio are such variables. Moreover, saturation cannot adequately or uniquely describe the flow conditions. This is because saturation alone brings no definite input to the momentum balance; therefore, it is questionable if it can provide any information on the kinetics of the macroscopic flow.

At flow conditions of "relatively small values" of the capillary number, the intermittent flow of disconnected NWP results in a relative reduction of the permeability of both the NWP and the wetting phase (WP). The population of disconnected fluidic elements blocks part of the cross section available to the flow by a fraction analogous not only to the average saturation but also to their stranding/mobilization probability. The collective interaction between the population of NWP fluidic elements and the WP flow triggers continuous, cascading pressure fluctuations that mobilize some of the stranded fluidic elements and result in intermittent flows.

Observations of single-phase flows within pore networks confirm that the macroscopic pressure gradient scales linearly with the superficial fluid velocity, as described by Darcy's law. Such linearity seems to be a quite trustworthy modeling consideration in the case of two-phase flow as well, but only when very high superficial velocities are considered, and capillary forces are negligible. However, at moderate/low velocities, when capillary forces are comparable to viscous forces, the macroscopic pressure gradient does not scale linearly with the flow rate. Experimental studies on steady-state two-phase flows in glass beads (Tallakstad et al., 2009; Aursjø et al., 2014; Datta et al., 2014), in glass bead columns (Sinha et al., 2017), as well as in sand-pack columns (Tsakiroglou et al., 2015), revealed that the nonlinear relation between the pressure gradient and the flow rate can be described by generic power laws with different exponent values. The discrepancy between the values of the scaling exponents is attributed to differences associated with the dimensionality of the pertinent variables, measurements pertaining to different flow conditions, dimensionality of the NWP/WP/PM system, etc. Therefore, it is worth the effort to examine if these "different" observations can be integrated into a universal power law relating appropriate, dimensionless variables of the process.

To this end, a first attempt at deriving a universal scaling functional form describing the flow dependency of relative permeability is proposed by Valavanides (2018c, 2023). It is based on the results from systematic, extensive simulations spanning five orders of magnitude for both the capillary number and flow rate ratio, implementing the DeProF

model algorithm, built around a hybrid, true-to-mechanism, stochastic scale-up model for steady-state two-phase flows in pore networks (Valavanides, 2018a).

In the present work, we apply the proposed flow rate-dependent relative permeability scaling model when immiscible, steady-state two-phase flows take place within artificial 2D microfluidic networks across different flow regimes. The objective is: (a) to examine the applicability of the proposed scaling across NWP/WP/PM systems of different sizes; (b) to verify the existence, uniqueness, and form of the locus of critical flow conditions, an inherent characteristic of such processes in terms of energy efficiency; (c) to examine any forensic characteristics, i.e., the potential for revealing the interstitial flow structure from ex-core measurements.

To do so, we performed a systematic laboratory study of steady-state two-phase flow in an artificial microfluidic pore network. Data were collected over a grid of flow conditions, spanning across four orders of magnitude on the capillary number, *Ca*, and up to three orders of magnitude on the flow rate ratio, *r*.

This article is divided into four sections. We start by providing the basic modeling assumptions for concurrent, immiscible, steady-state, two-phase flows in porous media and present the basic structure of the proposed flow-dependent relative permeability scaling ("Basic Theoretical Background"). We continue ("Materials and Methods") by describing the systematic, steady-state, relative permeability measurements we have taken in a microfluidic network. Then, ("Results and Discussion") we present the results of the laboratory study and discuss "points of agreement/disagreement" between scaling predictions and actual measurements, and we draw conclusions on the applicability of the proposed scaling or its potential exploitation in core analysis technology.

BASIC THEORETICAL BACKGROUND

Consider the simultaneous, one-dimensional concurrent flow of a nonwetting phase (NWP) and a wetting phase (WP). The variables pertaining to the NWP are indexed with *n*, whereas those pertaining to the WP are indexed with *w*. The compound flow is across a porous medium control surface, $\tilde{A}$, and induces flow rates equal to $\tilde{q}_n$ and $\tilde{q}_w$, respectively. Please keep in mind that a tilde (~) is used to indicate a dimensional variable; no tilde indicates a dimensionless one.

In general, as a result of the externally imposed flow rates, average corresponding pressure gradients, $(\Delta\tilde{p}/\Delta\tilde{z})_i$, $i = n,w$, are induced upon the two phases. The term average refers to the representative elementary volume (REV) average. This type of two-phase flow is conventionally described by the set of phenomenological, fractional flow, Darcy-type relations,

$$\frac{\tilde{q}_i}{\tilde{A}} \equiv \tilde{U}_i = \frac{\tilde{k}}{\tilde{\mu}_i} k_{ri} \left(\frac{\Delta\tilde{p}}{\Delta\tilde{z}}\right)_i \quad \frac{\tilde{q}_w}{\tilde{A}} \equiv \tilde{U}_w = \frac{\tilde{k}}{\tilde{\mu}_w} k_{rw} \left(\frac{\Delta\tilde{p}}{\Delta\tilde{z}}\right)_w, \tag{1}$$

where indices $i = n,w$ indicate the wetting phase (w) and the nonwetting phase (n), both incompressible, $\tilde{U}_i$ are the corresponding superficial velocities or flow rate intensities, $\tilde{k}$ is the absolute permeability of the pore network, $\tilde{\mu}_i$ are the dynamic viscosities of the two fluids, and $\tilde{z}$ is the length along the macroscopic flow direction.

The flow rate ratio, *r*, is defined as the ratio of volumetric fluxes,

$$r = \frac{\tilde{q}_n}{\tilde{q}_w} = \frac{\tilde{U}_n}{\tilde{U}_w}, \tag{2}$$

and the mobility ratio, λ, is defined as the ratio of the phase mobilities,

$$\lambda = \frac{\tilde{\lambda}_n}{\tilde{\lambda}_w} = \frac{\frac{k_{rn}}{\tilde{\mu}_n}\left(\frac{\Delta\tilde{p}}{\Delta\tilde{z}}\right)_n}{\frac{k_{rw}}{\tilde{\mu}_w}\left(\frac{\Delta\tilde{p}}{\Delta\tilde{z}}\right)_w} = \frac{1}{\kappa}\frac{k_{rn}}{k_{rw}}\frac{\left(\frac{\Delta\tilde{p}}{\Delta\tilde{z}}\right)_n}{\left(\frac{\Delta\tilde{p}}{\Delta\tilde{z}}\right)_w}, \tag{3}$$

where

$$\kappa = \tilde{\mu}_n/\tilde{\mu}_w \tag{4}$$

is the NWP/WP bulk viscosity ratio.

The average intrinsic capillary pressure is defined (Valavanides, 2018b) as

$$\tilde{p}_c(\tilde{z}) \equiv \tilde{p}_n(\tilde{z}) - \tilde{p}_w(\tilde{z}), \tag{5}$$

where $\tilde{p}_i(\tilde{z})$, $i = n,w$, are the average bulk pressures in the NWP and WP, respectively (see also Valavanides, 2023, Appendix I). This definition is in line with the definition provided by Bear (2018, Eq. 6.1.1). Note that Eq. 5 provides a measure of the capillary pressure jump across the two bulk phase pressures; it is attributed to the combined effect of Young-Laplace capillary forces acting across all NWP/WP menisci. So long as the NWP is disconnected, to a larger or smaller extent, $\tilde{p}_c(\tilde{z}) > 0$.

Non-Fully Developed and Fully Developed Flow

Consider the case of steady-state co-injection of two immiscible fluids in a natural core or an artificial model pore network. When the fluids are injected at constant flow rates, they switch from pure, fully saturated, independent, Poisseuille flow in a tube to a complex network flow mode whereby they interact with each other. Specifically, at the inlet ports, the NWP disconnects into fluidic elements of some size distribution. Then, downstream, both NWP and WP create a flow system of some interstitial structure of evolving NWP size distribution. The local flow has a steady-state time average configuration; nevertheless, this average configuration changes or better evolves or adapts as it moves downstream. During this structural evolution, the flow is considered to be "non-fully developed." If the network or the core is adequately long and relatively homogeneous, then far downstream, the inlet ports, the flow system eventually abides to an invariant structure. In that case, it is considered to be "fully developed." Yet, settling into a fully developed structure is not always possible and depends on the flow conditions, as well as the properties of the fluids and the pore network. There are many factors that regulate the evolution of the structure of this two-fluid system. Most critical is the role of the relative magnitude of the viscous forces over capillary forces (damping out any local fluctuations instigated by the capillary forces) as well as the length and homogeneity of the network.

Exhibits of interstitial flow transitions from non-fully developed to fully developed structures can be found in Aursjø et al., 2014 (Fig. 7), whereby two-phase flows within long Hele-Shaw bead packs have been studied. A similar trend is observed in ganglion dynamics simulations, whereby the evolution of different ganglion size distributions downstream entry ports resulted in the same, stable, fully developed distribution (Fig. 14 in Valavanides et al., 1998).

Now, if the two-fluid flow system evolves downstream into a fully developed structure, the local ensemble of pressure discontinuities across the NWP/WP menisci ("capillary pressure jumps") attains some time-averaged, fixed value. Consequently, the difference between the average bulk phase pressures, namely the average intrinsic capillary pressure, Eq. 5, remains unchanged along the flow direction, i.e.,

$$\frac{\mathrm{d}\tilde{p}_c(\tilde{z})}{\mathrm{d}\tilde{z}} \to 0 \quad \wedge \quad \left(\frac{\Delta\tilde{p}}{\Delta\tilde{z}}\right)_n \approx \left(\frac{\Delta\tilde{p}}{\Delta\tilde{z}}\right)_w. \tag{6}$$

Therefore, the phenomenological, fractional flow, Darcy-type relations that describe the steady-state, fully developed flow, whereby the pressure gradient ($\Delta\tilde{p}/\Delta\tilde{z}$) is common in both fluids, become

$$\widetilde{U}_i = \frac{\tilde{q}_i}{\tilde{A}} = \frac{\tilde{k}}{\tilde{\mu}_i} k_{ri} \left(\frac{\Delta\tilde{p}}{\Delta\tilde{z}}\right) \quad , \qquad i = n, w, \tag{7}$$

and, under such conditions, the common pressure gradient in both phases can be expressed in reduced form as

$$x = \frac{\Delta\tilde{p}/\Delta\tilde{z}}{(\Delta\tilde{p}/\Delta\tilde{z})^{1\Phi}} = \frac{\Delta\tilde{p}/\Delta\tilde{z}}{\tilde{\gamma}_{nw} Ca/\tilde{k}} = \frac{\Delta\tilde{p}}{\Delta\tilde{z}} \frac{\tilde{k}}{\tilde{\mu}_w \widetilde{U}_w} = \frac{1}{k_{rw}}, \tag{8}$$

where $(\Delta\tilde{p}/\Delta\tilde{z})^{1\Phi}$ is the pressure gradient corresponding to an equivalent saturated single-phase flow (1Φ) of the WP at the same superficial velocity, $\tilde{U}w$.

Ca is the capillary number, conventionally defined as

$$Ca = \tilde{\mu}_w \widetilde{U}_w / \tilde{\gamma}_{nw}, \tag{9}$$

where $\tilde{\gamma}_{nw}$ is the NWP/WP interfacial tension.

In Eq. 8, the actual pressure gradient is divided by the pressure gradient of an equivalent single-phase flow of the WP with a superficial velocity equal to $\tilde{U}_w$, which is the second component of the product. Note that, by definition, it is straightforward to verify that the reduced pressure gradient is essentially the inverse of the relative permeability of the WP (see far right side of Eq. 8). Moreover, the set of superficial velocities in Eq. 7 may be appropriately reduced and replaced by a set of dimensionless variables, namely, the capillary number, *Ca*, Eq. 9, and the NWP/WP flow rate ratio, *r*, Eq. 2.

At steady-state conditions when the flow is fully developed, i.e., there are either no capillary end effects or they can be considered to be negligible, the flow rate ratio, *r*, becomes equal to the mobility ratio, λ.

$$r = \frac{U_n}{U_w} \equiv \frac{1}{\kappa} \frac{k_{rn}}{k_{rw}} = \lambda \quad \Leftrightarrow \quad k_{rn} = \kappa r k_{rw} \tag{10}$$

The equivalence, expressed in the first part of Eq. 10, is a conjecture resulting from direct flow analysis (see Appendix I in Valavanides, 2018b) in case the flow is fully developed. Equation 10 is very useful, as we may easily recover the *r* value pertaining to any pair of measured $\{k_{rn}, k_{rw}\}$ values from a conventional relative permeability diagram. Therefore, switching to the concept of flow dependency may be readily applicable as conventional relative permeability diagrams can still be used, so long as it is confirmed that the flow system is free of capillary end effects.

In fully developed flows, because of the common pressure gradient, Eq. 7 or 8, and the equivalence between flux ratio and mobility ratio, Eq. 10, relative permeability

curves intersect at a fixed value of the flux ratio, the so-called relative permeability crossover flux ratio value, r_x. The latter is equal to the inverse of the viscosity ratio,

$$r_x = 1/\kappa \tag{11}$$

This inherent characteristic of steady-state, fully developed flows, Eqs. 10 and 11, may be used in assessing the presence of capillary end effects when reviewing SCAL data. If the imposed flow rate ratio values, r_i, and the corresponding measured mobility ratio values, λ_i, are equal, then fully developed flow conditions have settled in, and end effects are negligible. Ideally, if all co-injections take place with no end effects, then if all pairs of $\{r_i, \lambda_i\}$ are drawn on a log-log diagram, the corresponding markers align on a straight line with inclination 1:1. Yet, in practice, when SCAL measurements are examined, the equality expressed by Eq. 10 could be used as a soft criterion in verifying the absence of end effects. The markers from $\{r_i, \lambda_i\}$ pairs drawn on a log-log diagram should line up tightly on a straight line with inclination 1:1. If some markers do not conform, that is an indication of the presence of end effects at the corresponding co-injection experiments. R-squared measures could be used to provide an overall assessment of the conditions in which the SCAL measurements were taken. The trend is presented in a review of relative permeability vs. flux ratio diagrams by Valavanides et al. (2016). As we will see in the following "Results and Discussion," the same trend is generally also observed in the diagrams produced from the current study (Fig. 4), albeit the alignment is not universally observed, and some co-injections show not to be free of capillary end effects, so the corresponding flows are not fully developed.

Energy Efficiency and Independent Variables

In the present work, we will also analyze the results from an energy efficiency perspective. In this context, we will use the reduced, normalized measure of the energy efficiency of the process, considered as the flow rate of the NWP per unit of total hydraulic power spent or, equivalently, provided externally to the NWP/WP/PM system by the "pumps" to maintain two-phase flow—an essentially dissipative process—at any set of externally imposed flow conditions, *Ca* and *r*. The associated energy utilization factor, or energy efficiency index, f_{EU}, can be readily calculated in terms of macroscopic measurements (Valavanides, 2018b) as

$$f_{EU} = \frac{k_{rn}}{\kappa(r+1)} = \frac{rk_{rw}}{r+1} = \frac{r}{x(r+1)}. \tag{12}$$

An important characteristic of the sought process is that for every fixed value of the capillary number, *Ca*, there exists a single value of the flow rate ratio, r^*, for which the energy efficiency index, f_{EU}^*, attains a maximum value (Valavanides et al., 2016; Valavanides, 2018b). Moreover, for every NWP/WP/PM system, a unique locus of energy efficiency maxima is formed, $r^*(Ca)$. The flow conditions that correspond to the $r^*(Ca)$ locus and minimize the total energy dissipation per unit of NWP flow rate are called critical flow conditions (CFCs). The CFCs of an NWP/WP/PM system can be measured and identified in a straightforward manner by typical relative permeability measurements. The critical energy efficiency index, $f_{EU}^*(Ca)$, and the associated locus of CFCs, $r^*(Ca)$, provide a strong flow analysis and characterization tool (Valavanides, 2018b).

Closing this passage, we also need to address the issue of selecting and using the flow rate ratio, *r*, instead of the fractional flow of the WP, f_w, as one of the two independent variables of the process – the other being the capillary number, *Ca*. In the core-analysis community, the applicable standard is to refer to one of the fractional flows, by convention, that of the WP, f_w. Switching between *r* and f_w (or f_n) is readily provided through the transformation $f_w = r/(1 + r)$. Nevertheless, the use of the flow rate ratio, *r*, instead of the fractional flow, f_w, as the independent variable has the advantage of a more convenient description of the sought physical process, especially (or at least) around the critical flow conditions, whereby the identification of the critical flow rate ratio, log $r^*(Ca)$, becomes more evident. The acute peak, when *r* is used, is more precisely defined than the blunt one diffused over a broad plateau when f_w is used (Valavanides et al., 2016). As a general observation, all (f_{EU} vs. *r*) energy efficiency diagrams show a more uniformly smooth trend when compared to (f_{EU} vs. f_w) diagrams, irrespective of the particular values of the system parameters and flow conditions.

True-to-Mechanism Model of Steady-State Relative Permeabilities

The mechanistic model DeProF for immiscible, steady-state two-phase flow in pore networks may be used to predict the reduced macroscopic pressure gradient, *x*, given the flow conditions and system properties. The model is based on the concept of decomposition in prototype flows, hence the acronym DeProF. It takes into account the pore-scale mechanisms and the sources of nonlinearity caused by the motion of interfaces, as well as other complex, network-wide cooperative effects, to estimate—in a stochastic sense—the

conductivity of each class of pore unit cells. It implements effective medium theory with appropriate expressions for pore-scale-to-macroscale consistency for the NWP and WP mass transport to derive an implicit algebraic relation invoking the macroscopic pressure gradient, the capillary number, Ca, the flow rate ratio, r, the viscosity ratio, κ, the dynamic advancing and receding contact angles, (θ_A, θ_R), and a set of parameters that describe the geometrical, topological and structural characteristics of the pore network, $\boldsymbol{x}_{pm}$ (Valavanides, 2018a).

Using the DeProF model, one can obtain the solution to the problem of steady-state two-phase flow in porous media in the form of the following transfer function,

$$x = x(Ca, r; \kappa, \theta_A, \theta_R, \boldsymbol{x}_{pm}). \quad (13)$$

Implementation of the DeProF model is possible when analytical expressions of the pore network geometry are plausible and general expressions for the pore network unit-cell conductivities can be calculated for all possible flow configurations. In general, this is not the case for natural porous media, but only for a certain class of model pore networks with analytically tractable pore geometry. Yet, one can benefit by scanning entire domains of flow conditions at relatively short computational times and, therefore, get a systematic and consistent overview of the behavior of the flow across orders of magnitude of flow conditions. In that context, DeProF was used as a virtual SCAL simulator implementing large cores with unbiased measurements, thanks to the absence of capillary end effects because of the "infinite" length of the REV model streamtube.

Extensive simulations implementing the DeProF algorithm have been carried out in the past to derive maps that describe the dependence of the flow structure on the independent flow variables, namely the capillary number, Ca, and the flow rate ratio, r (Valavanides, 2018a). The simulations spanned five orders of magnitude in Ca ($-9 \le \log Ca \le -4$) and r ($-2 \le \log r \le 2$) over sufficiently fine steps, and fluid systems with various viscosity ratios (nine in total) have been examined.

Universal, Relative Permeability Scaling Form, Incorporating Flow Rate Dependency

Based on the DeProF model simulations, it was possible to infer a universal description of the dependence of the reduced pressure gradient, $x(Ca, r)$, on the capillary number, Ca, and the flow rate ratio, r, expressed by the universal scaling form (Valavanides, 2023),

$$x(\log Ca, \log r) = A(\log Ca) + \kappa r, \quad (14)$$

extending over orders of magnitude in Ca and r. The effects of capillarity and viscosity are partitioned in two decoupled terms. The linear term describes the fractional contribution of the bulk viscosities through the viscosity ratio, κ. The nonlinear term, $A(\log Ca)$, accounts for the contribution of capillarity at different flow conditions. That nonlinear term is the intrinsic dynamic capillary pressure (IDCP) function and describes the capillary effects associated with the physicochemical properties of the two-fluid system and the pore network, namely, wettability (dynamic receding and advancing contact angles) and pore network geometry. The relative contributions of those two terms depend on the flow conditions.

The IDCP function, $A(\log Ca)$, is a characteristic property of the NWP/WP/PM flow system. It depends on capillarity-related characteristics, i.e., the tripartite interaction between interfacial tension, wettability (dynamic advancing and receding contact angles), and the pore network geometry. The term dynamic in IDCP is used to indicate that capillary pressure is evaluated at different flow conditions, not in static equilibrium (Valavanides, 2023).

In the present study, we will repeat the procedure implemented in a similar SCAL study on a natural sandstone core (Valavanides et al., 2020) and try to recover an expression $A(\log Ca)$ specific to the NWP/WP/PM flow system under consideration.

MATERIALS AND METHODS

The laboratory study presented here comprised the simultaneous, continuous, steady-state, co-current injections of two immiscible fluids within a specially prepared microfluidic network for different flow conditions. The entire set of lab measurements comprised a total of 152 co-injections, organized in 12 groups of constant Ca values, covering an area of approximately four orders of magnitude on Ca and approximately three orders on r values.

Microfluidic Model and Fluids

A Poly-Di-Methyl-Siloxane (PDMS) micromodel was used as the pore network. The micromodel was produced in-house, following the principles of optical and soft lithography (Xia and Whitesides, 1998). The pore structure of the micromodel is depicted in Fig. 1.

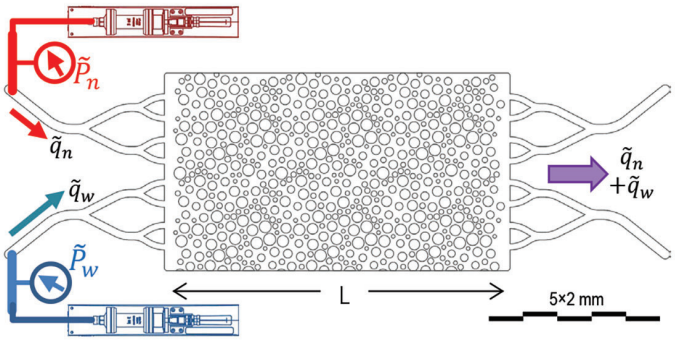

Fig. 1—Plane section of the microfluidic PDMS network showing the pore structure of the porous medium. The fluids are co-injected through the inlet microchanneling at left at predetermined fluxes; the immiscible flow outlet is through the microchanneling at right.

Circles correspond to the planar cross sections of the PDMS cylinders (solid pillars) connecting the two parallel plates confining the flow. The effective dimensions of the pore space are 10 × 20 mm. The depth of the porous structure is equal to 43 μm and is constant throughout the entire pore space. The pore network is periodic in both principal orthogonal directions. It is made by tiling up a basic network element in both directions: three periods along the longitudinal axis, which is also the superficial flow direction, and two periods across the transverse axis. The pore size range is 75 to 250 μm, with a mean size equal to 180 μm. That range pertains to the diameters of circles inscribed in the various pores; the latter comprise the void space between the aforementioned cylindrical pillars ("grains"). Because of the particular geometric configuration, there is no clear/nominal characterization of pore bodies as "chambers" or "throats." A conventional dimensional delimiter could be the average diameter of inscribed circles; any pore with a larger nominal diameter could be considered a chamber, whereas a pore with a smaller nominal diameter a throat. As per connectivity, there are no dead-end pores apart from those residing at the sides of the network parallel to the longitudinal flow direction. For the record, the network with this particular geometry is referenced as "Netwk22."

The surface of the cross section (perpendicular to flow) is estimated at $\tilde{A} = 4.3 \times 10^{-7}$m^2. The absolute permeability, taking into account the inlet/outlet microchannel network, was measured at $\tilde{k} = 8.1 \times 10^{-11}$m^2. The two immiscible fluids are injected through the inlet microchanneling at the left part of the network and with predetermined fluxes, $\tilde{q}_n$, $\tilde{q}_w$. The immiscible flow exits the network through the outlet microchanneling at the right.

The fluids used in the experiments were deionized water dyed with ink as the nonwetting phase (NWP) and Fluorinert™ FC-770 as the wetting phase (WP). The addition of the dye in water has practically no effect on its viscosity and density, as confirmed by relevant measurements. The basic properties of the fluids are presented in Table 1.

The wettability of the two-fluid and PDMS system is described by the dynamic advancing and receding contact angles, with nominal values roughly estimated from visual observations of the recorded snapshots at $\theta_A = 54 \pm 5$ deg and $\theta_R = 45 \pm 5$ deg, respectively.

Experimental Setup and Procedure

For the simultaneous injection of both fluids at independent volumetric fluxes, two CETONI™, neMESYS 1000N syringe pumps were used, one for each fluid. The syringe pumps were combined with a BASE120 module. With this setup, it was possible to inject the fluids at volumetric fluxes as low as a few microliters per minute (10^{-3} ml/min) to maintain a capillary-dominated flow regime, up to milliliters per minute (ml/min), to sustain viscosity-dominated flow regimes. The inlet pressure of each phase was measured with a variety of Elveflow™ MPS sensors, depending on the values of the expected pressure buildup during the injection and the desirable/acceptable measurement accuracy. Both the syringe pump and logging of the pressure readout values were controlled with QMixElements™. Sampling and recording of the pressure values at the inlet port for each phase were set at rates between 0.5 and 10 Hz, depending on the flow conditions and the expected speed of events.

Table 1 —Basic Physicochemical Properties of the Fluids Used in the Study

Fluid	Density, $\tilde{\rho}$ (Kg/m^3)	Dynamic Viscosity, $\tilde{\mu}$ (mPas)	Interfacial Tension, $\tilde{\gamma}_{nw}$ (N/m)
Fluorinert™ FC-770 (WP)	1,793	1.359	55×10^{-3}
Deionized Water + Dye (NWP)	1,000	1.00	

In order to be able to assess whether or not the process has reached an interstitially steady state, the entire flow system was visualized using an open-air microscope, a modification of the one introduced by Karadimitriou et al. (2013), whereby a single camera was used for the visualization of the entire network instead of four. The camera used was a monochrome Basler™ 5 Mpx, 23 fps, acA2440-20gm. The purpose of visualizing the interstitial flow was to cross-check the structure of the flow, the readouts from the pressure transducers, and the injected fluxes. There was no video recording but simple snapshot capturing. Frame rate varied from 15 to 1 Hz, depending on the speed of the process, at a resolution of around 8 μm/pixel, which was adequate to observe pore-scale events.

Procedure Followed for Each Experiment. With the term "experiment," we refer to a complete cycle of co-injecting the two phases at constant WP flux but with successive increases of the NWP flux. For every experiment, a fixed capillary number value, Ca_i, i = 1,…,12, is maintained, whereas the flow rate ratio takes successive values, r_j, spanning across a domain between 0.1 and 10. The domain of flow conditions in the entire set of experiments is depicted in Fig. 2.

Each of the 12 constant-*Ca* rows is associated with corresponding diagrams in Figs. 4, 6, 7, 8, and 9a.

The typical cycle in every experiment comprises the following interventions:

- The micromodel is initially saturated with the wetting phase, Fluorinert™. Then, both phases are injected into the microfluidic network.
- The WP is injected at a fixed volumetric flux to maintain a constant value of the capillary number, *Ca*, during the entire cycle of the experiment.
- The volumetric flux of the NWP starts at approximately one-tenth of the WP flux, and it is increased in successive steps (about 9 to 12) to 10 times larger; the result is approximately three orders of magnitude in successive increments. Initial co-injection is considered as primary drainage type (these lay on the dashed line in Fig. 2). Successive co-injections at increasing steps of constant volumetric flux of the NWP are considered as secondary drainage type. There are two particular experiments that need to be referenced:
  - Experiment No. 7, run at $Ca = 3.83 \times 10^{-5}$, was repeated to check repeatability; this is indicated by a set of smaller circle markers in Fig. 2.
  - In Experiment No. 8, pertaining to $Ca_8 = 4.79 \times 10^{-5}$, the flux of the NWP was increased $r_j \in \{0.2, 1.0, 2.0, 10.0\}$ and then decreased, $r_j \in \{10.0, 8.0, 5.0, 0.8, 0.2\}$; therefore, the co-injection type evolved from drainage (○) to imbibition (△) (see detail in Fig. 2).
- After each step-up of the NWP flux, an adequate period of time is allowed for the interstitial flow to reach a steady state.

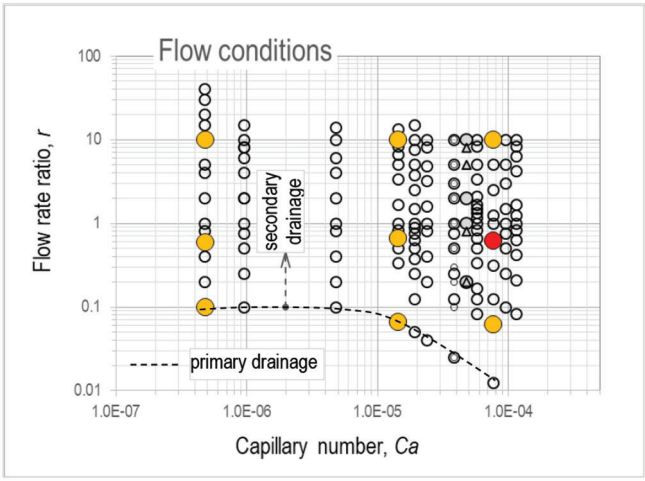

Fig. 2—The domain of steady-state flow conditions examined in the study. Markers indicate values of the capillary number, Ca_i, and flow rate ratio, r_j. The dashed arrow indicates the progressive increase of the flow rate of the NWP (at fixed Ca_i) for all experiments. The solid markers identify flow conditions pertaining to the diagrams in Fig. 3 (in red) and Fig. 5 (in yellow).

- As soon as the time-averaged pressure values showed signs of stabilization for both phases (kinetic stabilization), the entire microfluidic network was visually inspected in order to cross-check that the interstitial flow was also stabilized, or any fluctuations showed some kind of sustainable, short-cycle periodicity. In most of the cases, a steady value for the pressures would come along with a stabilized flow, judging from visual inspection of the interstitial flow (changes in saturation, migration of menisci, and other pore-scale phenomena). Occasionally, and most frequently for low volumetric fluxes of the NWP, we observed periodic fluctuations and/or oscillations over the pressure readouts for both phases, which would always be accompanied by snap-off events within the pores. In these cases, the system was left to oscillate for a few periods to identify the characteristics of the oscillation, e.g., actual period and wavelength (see an indicative case in Fig. 3, whereas a systematic trend is presented in the diagrams in Fig. 5).
- Following the establishment of steady-state conditions in the interstitial flow, the volumetric flux of the nonwetting phase is stepwise increased.

- After successive repeats with progressive stepwise increments of the volumetric flux of the NWP, the latter would have reached values ~10 times the value of the WP, corresponding to a flow rate ratio value, $r = 10$. Then, the experiment for that particular constant-Ca value stops.
- The system has then to be reconfigured to accommodate the next set of steady-state two-phase flows at a different constant-Ca value (constant q_w value). A new experiment pertaining to a new Ca value, repeating a new cycle as described above, is deployed.

Data Logging and Management

For each run at constant $\tilde{q}_n$ and $\tilde{q}_w$, the values of flow rates and gauge pressures at the inlet ports for each phase were sampled at predetermined rates and recorded (see previous subsection). The recorded data were graphically plotted. Endpoint (steady-state) pressures were estimated from these plots by time averaging.

A typical evolution of the two flow rates and pressures at the inlet ports is depicted in the diagram in Fig. 3. Please note that the time axis (horizontal) and the flux axis (vertical, right) are logarithmic, whereas the pressure axis (vertical, left) is linear. Pressure values are indicated by markers; fluxes are indicated by lines.

The endpoint pressure values are calculated by time averaging over a selected interval. This interval, whereby interstitial steady state is reached, is delimited by the two "×" markers. Delimiting this time interval for every examined flow setup (Ca, r) follows after identifying some form of stabilization in the corresponding pressure log diagram. Then, the average endpoint (steady-state) pressures, $\langle\tilde{P}_n\rangle$,$\langle\tilde{P}_w\rangle$, are automatically calculated by simple averaging over the corresponding time interval. These values are displayed in Table A1.1 in Appendix 1 of the paper, Columns 6 and 7 for the entire set of examined flows. The pressure gradients for the WP and the NWP are then readily calculated as

$$\left(\frac{\Delta\tilde{p}}{\Delta\tilde{z}}\right)_i = \frac{\langle\tilde{P}_i\rangle}{L}, \qquad i = n, w. \tag{15}$$

For example, for the flow setup pertaining to Fig. 3, the endpoint stage pressures are averaged over the time interval $40s \le t \le 80s$, as indicated by the pair of the large cross markers (×).

The pair of pressure gradient values per phase, $\{(\Delta\tilde{p}/\Delta\tilde{z})_n,(\Delta\tilde{p}/\Delta\tilde{z})_w\}$, was then used to calculate the corresponding pair of relative permeability values for the NWP and WP, $\{k_{rn}, k_{rw}\}$, from Eq. 7.

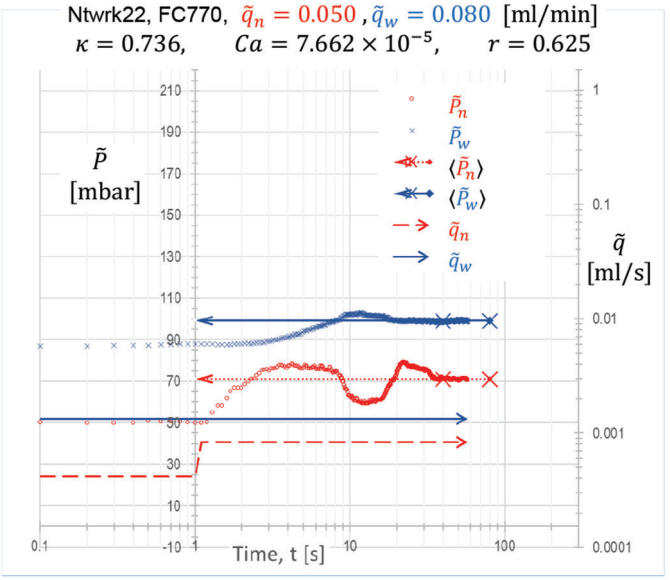

Fig. 3—Time evolution of the inlet pressure for a typical co-injection of the two phases at predetermined volumetric flow rates. The compact line (blue,_____) indicates the volumetric flow rate for the WP, $\tilde{q}_w$, dashed line (red,_ _) for the NWP, $\tilde{q}_n$ (the step indicates the imposed increase in volumetric flow rate succeeding the previous co-injection setup). The time evolution of the measured pressure at the inlet port of the NWP is indicated by the small circle markers (red, ○); the pressure evolution at the WP inlet port is indicated by the small cross markers (blue, ×). The long horizontal arrows indicate the average pressure values calculated when interstitial steady-state conditions settle in; averaging is taken over the time interval delimited by the large crosses (see main text for details).

We need to stress here that we have considered the general condition that the flow may not be fully developed; therefore, the NWP and WP pressure gradients would not necessarily be equal. In such general condition, $(\Delta\tilde{p}/\Delta\tilde{z})_n \neq (\Delta\tilde{p}/\Delta\tilde{z})_w$, therefore

$$k_{rn} = \tilde{\mu}_n\tilde{U}_n\Big/\left[\tilde{k}\left(\frac{\Delta\tilde{p}}{\Delta\tilde{z}}\right)_n\right] = \tilde{\mu}_n r\tilde{U}_w\Big/\left[\tilde{k}\left(\frac{\Delta\tilde{p}}{\Delta\tilde{z}}\right)_n\right]$$
$$k_{rw} = \tilde{\mu}_w\tilde{U}_w\Big/\left[\tilde{k}\left(\frac{\Delta\tilde{p}}{\Delta\tilde{z}}\right)_w\right]. \tag{16}$$

To test if the flow is fully developed (at the endpoint stage), we have calculated the mobility ratio, Eq. 3, pertaining to the relative permeability values obtained from Eq. 16.

After reviewing some preliminary results, we have decided to recalculate the energy efficiency values based on the same structure as of the original/nominal expression, Eq. 12, but using the mobility ratio values,

$$f_{EU} = \frac{\lambda k_{rw}}{\lambda+1}, \tag{17}$$

instead of the flow rate ratio values, r. In that context, it was more descriptive—in terms of the physics of the interstitial flow—to use the "kinetic" (Eq. 1) rather than the "kinematic" (Eq. 12) definition of the energy efficiency index.

At the end of the day, we have created an extensive database in the form of a look-up table with sets of calculated values corresponding to measurements for the entire ensemble of flow conditions. The entire set of calculated values of endpoint pressures per (Ca, r) flow setup is displayed in Table A1.1 in Appendix 1. Please note that the entire data set is grouped into data subtables pertaining to constant-Ca flows. The entire data set of measurements, comprising the time evolution of the inlet gauge pressure for each phase and the corresponding fluxes, is available at the Data Repository of the University of Stuttgart (DaRUS) (DOI: 10.18419/darus-2816).

RESULTS AND DISCUSSION

Pairs of NWP and WP relative permeability values $\{k_{rn}, k_{rw}\}$, were calculated using Eq. 16 for each measurement. The collected relative permeability values are plotted against the corresponding values of the flow rate ratio, r, into diagrams pertaining to the 12 constant-Ca experiments. These diagrams are presented in Fig. 4. The relative permeability values of the NWP and WP, k_{rn} and k_{rw}, are indicated by red squares and blue triangles, respectively. In every constant-Ca diagram, we have also plotted values of the mobility ratio, λ, calculated using Eq. 3, as well as values of the energy efficiency f_{EU}, calculated using Eq. 17, against the values of the flux ratio, r.

Note that in all the constant-Ca experiments, the imposed flow rate ratio was increased from 0.1 or 0.01 to 80 or 10 in successive steps of a single pass. So, in every experiment, the co-injections are characterized as primary drainage type to secondary drainage type. In all constant-Ca diagrams, the flow rate ratio is unidirectionally scanned from left (low r) to right (high r). There is only one exception. The experiment at $Ca_8 = 4.79 \times 10^{-5}$ was run at increasing r (primary to secondary drainage co-injection) and then at decreasing r (secondary imbibition co-injection) flow rate ratio (see the path followed on the middle diagram in the third line in Fig. 4). The corresponding snapshots captured at a frame rate of 1 Hz, are available in MP4 format at the DaRUS, DOI: 10.18419/darus-2816 (temporarily accessible via http://users.uniwa.gr/marval/HydroLab/FC770_k0736_Ca479e-5_20220209_snpsts0001-1181.mp4).

Non-Fully/Fully Developed Flow

By reviewing the diagrams in Fig. 4, we may check if the flows are fully or non-fully developed. Please note that the markers (×) indicating values of the mobility ratio, λ_i, against, r_i, are—in general—aligned along a straight line with gradient 1:1. In many cases, the two values are practically equal, i.e., $\lambda_i = r_i$. For those cases, the kinetic states of the interstitial flow structures, λ_i, are consistent with the externally imposed kinematic constraints, r_i, indicating that the corresponding flows are fully developed. Yet, focusing on the low-Ca regime, i.e., on the upper left diagrams, we may observe a significant discrepancy between the mobility ratio and the flow rate ratio, manifested as a failure of the $\{r, \lambda\}$ markers to perfectly align to the $r = \lambda$ straight line. The source of this discrepancy can be traced back to the capillary end effects that are induced by the relatively stronger role of the menisci when compared to the effects of the bulk viscosity. For those cases, we expect that the kinetic state of the interstitial flow structure is not fully consistent with the corresponding, externally imposed, kinematic constraint, and the corresponding interstitial flow has not reached a fully developed structure (see discussion on Eqs. 10 and 11 in "Non-Fully Developed and Fully Developed Flow").

In the same context, in many diagrams in Fig. 4 pertaining to different constant-Ca experiments, the lines connecting the NWP and WP relative permeability markers intersect at the so-called relative permeability crossover flux ratio value, $r_x = 1/\kappa$, as provided by Eq. 11. That value is delineated in all diagrams in Fig. 4 by the vertical dashed line.

Also note that in every constant-Ca diagram in Fig. 4, energy efficiency, f_{EU} (●), increases with increasing flux ratio, reaches a maximum value, and then decreases. The trend is universal in all diagrams. These maximum energy efficiency values increase with increasing Ca. The flux ratio values, for which the energy efficiency attains a maximum value, i.e., the critical flow rate conditions, tend to decrease with increasing Ca (compare diagrams from left to right, top to bottom). These findings are also presented in Fig. 9.

Interstitial Flow Instabilities at Flow Rate Step-Ups

In the course of the lab study, we have also observed another interesting systematic behavior: pressure fluctuations measured at the inlet ports. The fluctuations are triggered after a step-up in the flow rate ratio. An overview of the pressure evolution for indicative flow conditions is presented in the diagrams of Fig. 5. The diagrams are tabulated on a 3 × 3 layout.

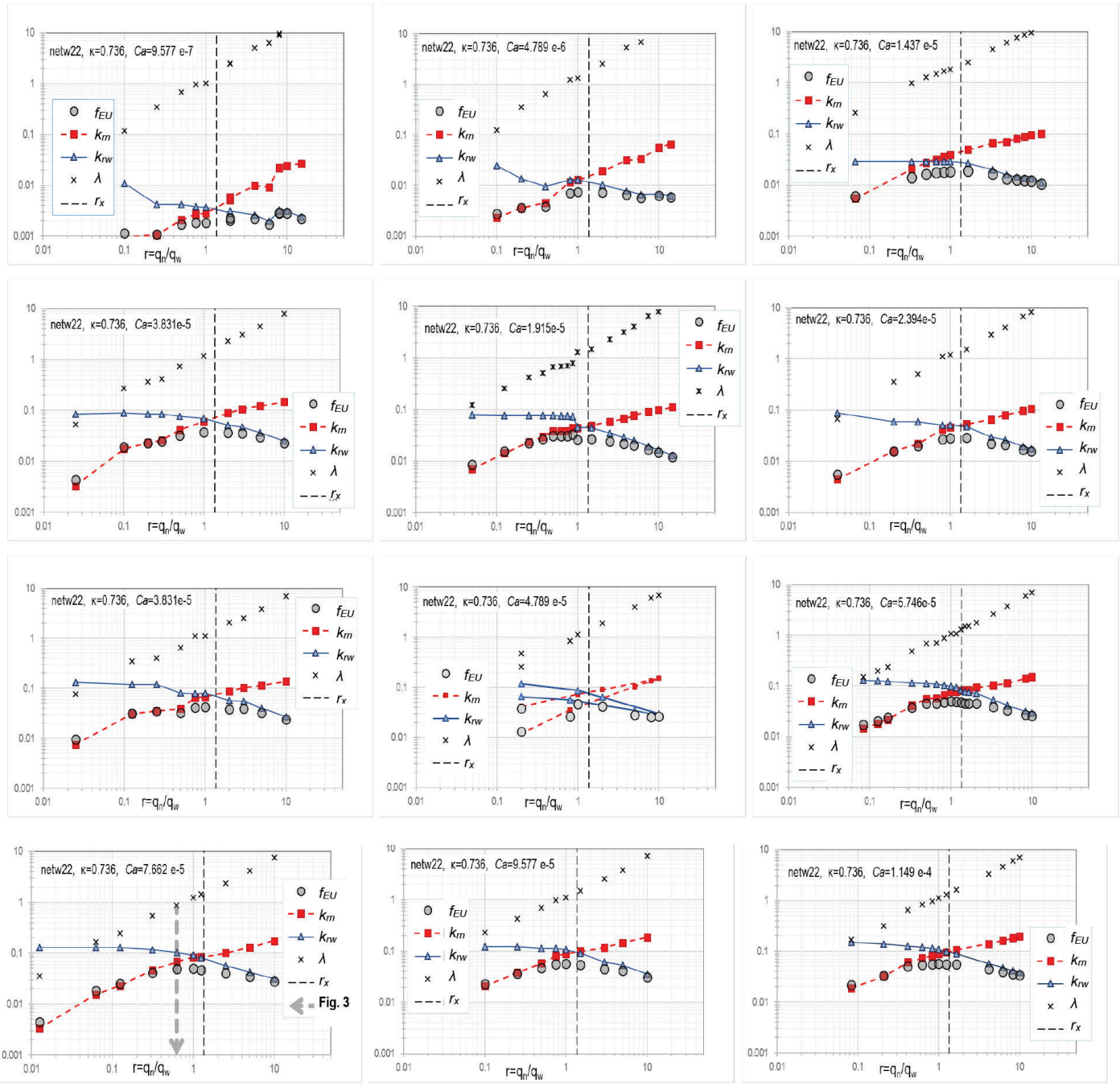

Fig. 4—Relative permeability (■,▲), energy efficiency (●), and mobility ratio (×) diagrams in the flow dependency format. Each diagram is associated with successive runs under a constant-*Ca* value. The straight, dashed, vertical lines indicate the theoretical value of the relative permeability crossover flux ratio value, as predicted by Eq. 11. The dashed thick line (gray) in the diagram at the bottom left corner identifies calculated values pertaining to the time evolution of the inlet pressures in the diagram of Fig. 3 (also referred to in Table A1.1).

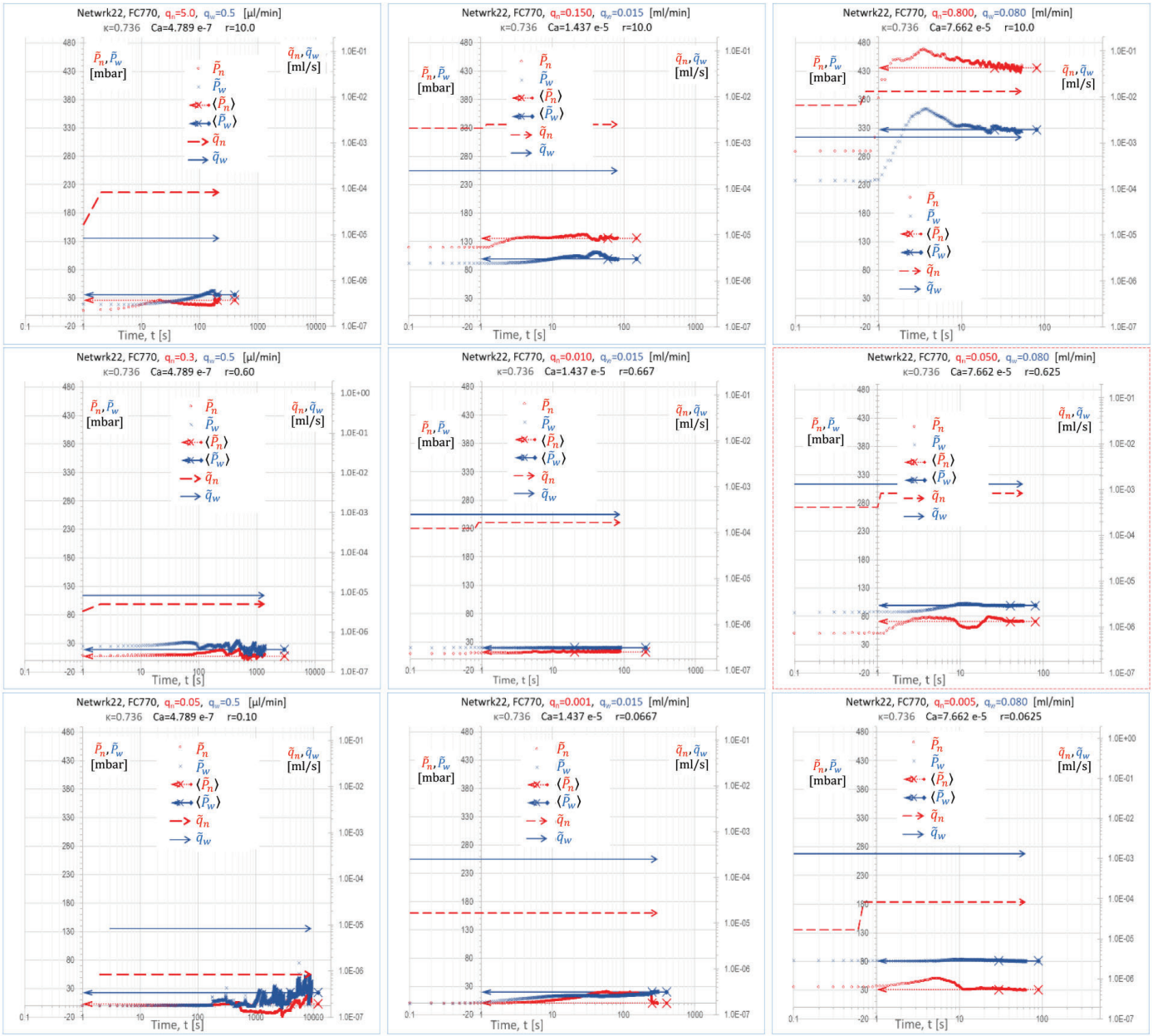

Fig. 5—Time evolution of the inlet pressure for typical co-injections of the two phases at different predetermined volumetric fluxes. (Flow conditions pertain to those indicated in Fig. 2 by the filled markers.) The compact line (blue, ___) indicates the volumetric flux of the WP, $\tilde{q}_w$, dashed line (red, _ _) for the NWP, $\tilde{q}_n$. The step indicates the imposed increase in volumetric flux succeeding the previous co-injection. The time evolution of the measured pressure at the inlet ports of the NWP and the WP are indicated by the small circle markers (red, ◯) and the small cross markers (blue, ×), respectively. The arrows to the left axis indicate the pressure values reached when steady-state conditions settle in (see main text for details).

Each column pertains to constant-*Ca* experiments, *Ca*~4.8 × 10^{-7}, 1.4 × 10^{-7}, 7.7 × 10^{-5}, the flow rate for capillarity-dominated, capillary/viscous, and viscosity-dominated flows, respectively. Each row pertains to injections at equivalent flow rate ratios, *r*~0.07, 0.7, 10. The diagrams in Fig. 5 pertain to flow conditions marked in the diagram in Fig. 2 by the filled markers. The pressure fluctuations evolve with time as the process attains an almost fully developed interstitial flow structure, from the onset or step-up in co-injection flow rate ratio, *r*, to the point where

dynamic equilibrium settles in. The characteristics of these fluctuations (period, decay time, phase difference between $\tilde{P}_n$ and $\tilde{P}_w$) seem to depend on the imposed flow conditions (Ca, r). In most cases, the stabilization of the inlet pressures of the two phases is simultaneous. Following visual inspection (changes in saturation, migration of menisci, and other pore-scale phenomena), stabilization of the inlet pressures comes along with a stabilized structure of the interstitial flow. Occasionally, for low volumetric fluxes of the NWP, flow rate low-*Ca* values, we observe periodic fluctuations and/or oscillations over the pressure readouts for both phases, which are always accompanied by snap-off events within the pores. In these cases, the system is left to oscillate for a few periods to identify the characteristics of the oscillation, e.g., actual period and wavelength (see indicative diagrams in Fig. 5, left column, bottom).

Overall, we observe a systematic behavior, showing different degrees of attenuation, which indicates dynamic similarities to a multimodal spring/damper/mass oscillating system. In that context, the interstitial flow oscillations are due to the interplay between (a) the densities of the two fluids, (b) the relative magnitudes of the capillary (Young-Laplace) forces exerted by the NWP/WP menisci, (c) the energy dissipation due to the viscosities of the NWP and WP, as well as the hysteretic behavior of the menisci, due to differences on the dynamic advancing and receding contact angles within the atypical network geometry. The interplay is regulated/biased by the geometry of the pore network. The attenuation of the interstitial flow oscillations can vary from underdamped through critically damped to overdamped, indicating the response of the system depends on the changes or perturbations in the externally imposed flow conditions. We may infer that these different modes of attenuation and system response would also depend on the viscosity ratio of the system.

In general, our observations are in line with those reported in a work on interstitial flow fluctuations in natural cores (Rücker et al., 2021). The systematic structure of the interstitial flow oscillations indicates the potential for applications in flow and NWP/WP/PM system characterization, e.g., ex-core flow characterization, rock typing, etc.

Flow Rate Dependency of Relative Permeability

We may now proceed with revealing the proposed "flow-dependent relative permeability scaling for steady-state two-phase flow" for the microfluidic network flow setup.

Considering that the flow is fully developed, we have calculated the reduced pressure gradient, $x = 1/k_{rw}$ flow rate, the inverse of the relative permeability of the WP using Eq. 8. The entire set of x values is plotted in terms of the flow rate ratio, r, in Fig. 6, and in terms of the capillary number, Ca, in Fig. 7.

In Fig. 6, the values of reduced pressure gradient, x, are displayed in terms of log$r$, in groups of constant-Ca values. Please note that, with increasing r, there is an obvious asymptotic trend in aligning to the dashed, inclined line towards a virtually decoupled flow state. That is described by:

$$\text{As } r \to \infty,\ \log x = \log\kappa + \log r \ \Leftrightarrow\ x = \kappa r. \tag{18}$$

The inclination of the dashed line in the log-log diagram (Fig. 6) is equal to 1:1, and its pivot (marked by ○) is at point $\{r, x\} = \{r, \kappa r\} = \{1, 0.736\}$. The trend for all iso-*Ca* groups of x-value markers is similar to the trend observed in the DeProF model simulations (Valavanides, 2023) pertaining to a virtual sandstone network model. The same trend is observed in a similar diagram pertaining to the lab study on a natural sandstone core (Valavanides et al., 2020). We need to remind here that this asymptote describes or better delineates the domain of flow conditions whereby the compound flow resistance, attributed entirely to the bulk phase viscosities, is partitioned on complementary volume fraction rations (aka saturation). And it is at those high flow rate conditions (high Ca) that relative permeabilities can be expressed in terms of saturation in a "saturation-dependency" fashion.

In Fig. 7, the same values of reduced pressure gradient, x, are displayed in terms of logCa, lined up in rows of constant Ca. Within the same row, markers depict different values of the flow rate ratio, r. Note here, as we did not run all experiments on the same flow rate ratio values, it was not possible to group the x-values into r-classes. Also note, the × markers indicate the secondary drainage type co-injections pertaining to the $Ca_8 = 4.79 \times 10^{-5}$ experiment (middle diagram, third line, Fig. 4).

Although not quite obvious, there is a tendency (a confluence) of the markers to converge and align, in an asymptotic manner, towards the inclined, dashed line (in red). The trend is described by:

$$\log Ca \ll 0, \log x = \log\kappa - \log C_{pm} - \log Ca \\ \Leftrightarrow x = \kappa/\left(C_{pm} Ca\right) = 1/\left(Ca_{pm} Ca\right). \tag{19}$$

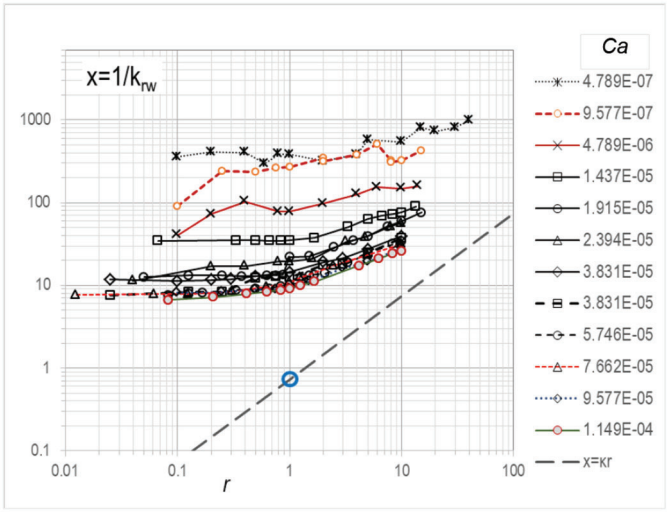

Fig. 6—Reduced pressure gradient values, *x*, in terms of the flow rate ratio, *r*, grouped into constant-*Ca* experiments.

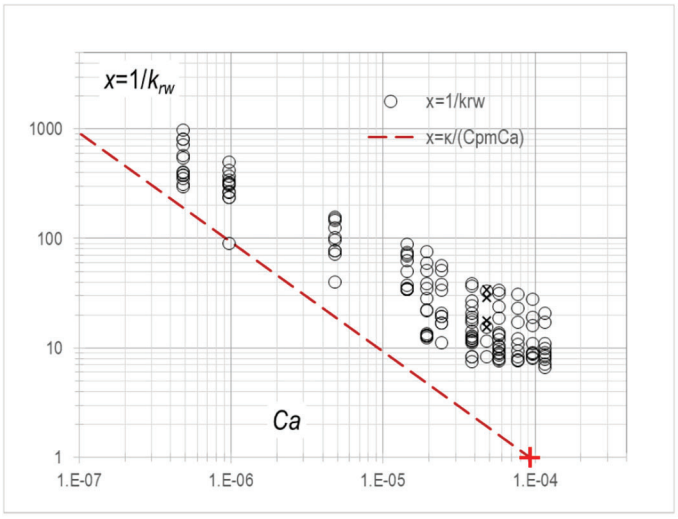

Fig. 7—Reduced pressure gradient values, *x*, in terms of the capillary number, *Ca*.

The functional form of this asymptote is given by an expression up to a constant value, C_{pm}, associated with the NWP/WP/PM system (Valavanides, 2023). The line asymptote has a negative inclination equal in measure to 1:1. For the particular set of data displayed in Fig. 7, we have used an arbitrary, best-guess, constant value $\log C_{pm} = 3.9$ to pivot the line along the *Ca* axis at $Ca_{pm} = \kappa / C_{pm} = 0.736/10^{3.9} = 9.266 \times 10^{-5}$.

By increasing this value but keeping the negative inclination equal to 1:1, the line is transferred in parallel to the left, at lower *Ca* pivot points, and vice versa. To estimate a more precise C_{pm} value, we need to have more data, and, most importantly, the data should mostly pertain to capillarity-dominated flows, i.e., for flow rate of the WP at lower *Ca* values close to the confluence region. The recovery of the correct C_{pm} value for a certain system is essentially a "dynamic network-typing" (as in "dynamic rock-typing") procedure. That is because the value of C_{pm} is associated with the interaction between the structure of the pore network and the wettability of the two-fluid system against the network surface, expressed by the dynamic advancing and receding contact angles.

Reveal of the Relative Permeability Scaling Incorporating Flow Rate Dependency

In order to describe the steady-state two-phase flow in the particular microfluidic system, in the form of the universal scaling function in Eq. 14, we need to reveal the associated kernel function, $A(\log Ca)$, namely the intrinsic dynamic capillary pressure (IDCP) curve (Valavanides, 2023). To this end, we will implement a fitting procedure using the available data.

We start with the implicit definition of $A(\log Ca)$ through Eq. 14 to get:

$$A(\log Ca) = x(\log Ca, \log r) - \kappa r \tag{20}$$

and then tap on the available reduced pressure gradient x_i values (i = 1, …,152) collected from the experiments for different *r* values. Eq. 20 is recast to a data format:

$$A_i = A(\log Ca_i) = x_{ij} - \kappa r_j. \tag{21}$$

We plot the calculated A_i values in terms of *Ca* in Fig. 8. The small black circles mark the IDCP values, A_i, aligned into rows of constant-*Ca* groups. Average values of *A* per constant *Ca* are marked with large red circles. These values are fitted by a power law. The power law fit indicates that $A(\log Ca)$ should asymptotically decay to zero at very large *Ca* values ($A \overset{Ca \to \infty}{\to} 0$). Yet, this is something that needs further investigation and verification. There are some structural limitations in the particular type of PDMS microfluidic model pore networks. At relatively large *Ca* values, the internal pressure increase—due to bulk viscosity-induced resistances—deforms the geometry of the relatively soft PDMS matrix (Gervais et al., 2006). That, on its turn, is expected to increase not only the effective porosity and absolute permeability but also the network geometry per se. Porosity has no impact, nor does the

absolute permeability, $\tilde{k}$, as the latter is used in reducing the analysis into dimensionless form (see Eq. 8). Yet, distortions in the network geometry may have a profound effect due to capillarity/wettability, especially so in low-*Ca* regimes. Consequently, that effect may question the consistency of characterizing the flow system if extreme flow conditions (at the very low-*Ca* domain) are imposed.

Energy Efficiency and Critical Flow Conditions

To reveal any latent systematic trends and eventually get a better image of the interstitial flow structure, we have also performed the energy efficiency analysis of the flow within the particular NWP/WP/PM system. The diagrams in Fig. 9 provide an overview of this analysis as it is implemented in this type of process.

In particular, the diagram in Fig. 9a displays a cascading set of energy efficiency values attained at every constant-Ca_i experiment, $\{r_j, f_{EU,\ ij}\}$. These are marked by small hollow circles. Each row of constant-Ca_i markers is associated with circle markers, $\{r_j, f_{EU,\ ij}\}$, at the corresponding constant-Ca_i diagram in Fig. 4.

For every constant-Ca_i row, a maximum value of energy efficiency is detected from trends in energy efficiency values observed in the diagrams in Fig. 4. That is implemented also taking into account the explicit values of f_{EU} in Column 13, Table A1.1. In that context, the f_{EU} maxima, each per constant-Ca_i experiment, are detected by:

$$f^*_{EU,i} = f^*_{EU}(Ca_i) = \max_j\{f_{EU,ij,}, Ca_i\}. \tag{22}$$

These are marked by larger filled circles. These maxima are connected with a dashed line. A remarkably smooth increase of the maximum energy efficiency values, f^*_{EU}, with increasing *Ca*, is observed. Moreover, it is worth noting that, depending on the flow conditions, the maximum energy efficiency of the process may increase by two orders of magnitude. That is quite an important characteristic when designing this type of process operation-wise. The maximum values (filled circle markers) tend to reach a maximum value—the so-called "ceiling of efficiency"—as proposed by Valavanides (2018b). Based on the energy efficiency analysis presented in that study, the maximum attainable value of the energy efficiency cannot exceed a value dictated by the viscosity ratio of the system, κ. This value is estimated to be equal to

$$f^*_{EU\infty} = \frac{1}{\left(1+\sqrt{\kappa}\right)^2} = \frac{1}{\left(1+\sqrt{0.736}\right)^2} = 0.2897$$
$$\Rightarrow \log f^*_{EU\infty} = -0.5381. \tag{23}$$

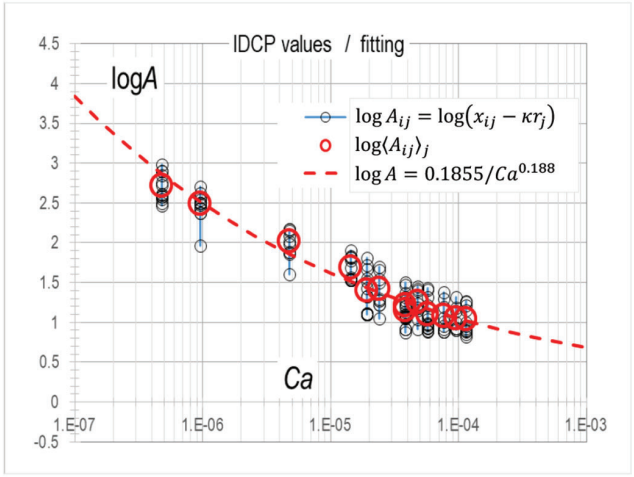

Fig. 8—Intrinsic dynamic capillary pressure (IDCP) values A_i, aligned into constant-*Ca* groups (small circles). Large red circles mark average *A*-values per constant *Ca*, fitted by a power law curve.

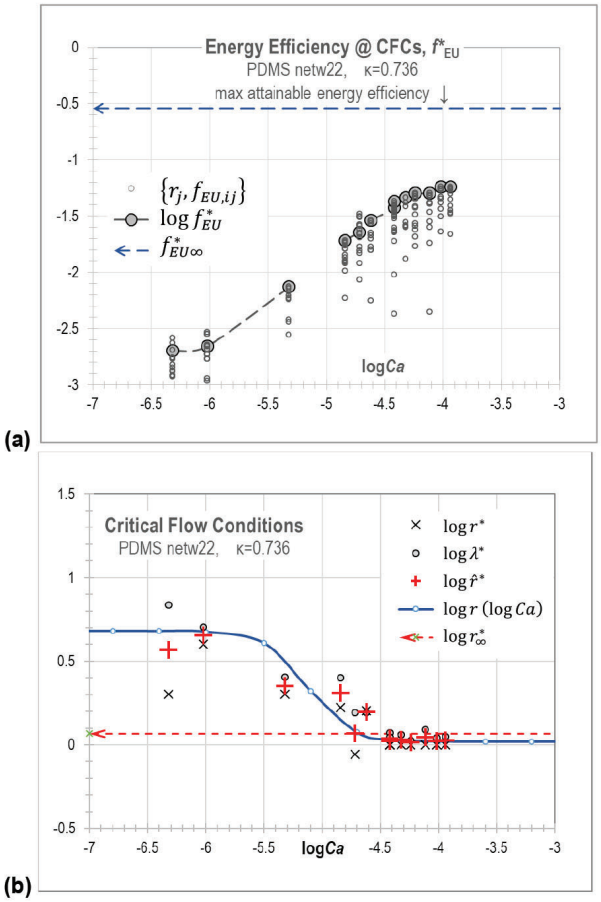

Fig. 9—(a) Energy efficiency values $\{r_j,\ f_{EU,\ ij}\}$,○, at different capillary number values and detected set of maximum values $\{Ca_i, f^*_{EU,i}\}$, ●, for the i = 1,..,12 constant-Ca_i experiments. (b) The corresponding critical flow rate ratio values, $\{Ca_i, r^*_i\}$, ×, and mobility ratio values, $\{Ca_i, \lambda^*_i\}$, ●, define the so-called critical flow conditions (CFCs); upright cross markers (in red +) indicate the mean value of the corresponding flow rate ratio and mobility ratio values, $\hat{r}^*$, Eq. 24.

We observe that the calculated values of energy efficiency tend to have reached a maximum value significantly lower than the expected limit (the ceiling of efficiency). This discrepancy is attributed to a bias of the measured value of the absolute permeability of the microfluidic pore network due to the inlet and outlet microchanneling (Fig. 1). Its nominal value is measured to be $\tilde{k} = 8.1 \times 10^{-11}\text{m}^2$, while some assumptions are made for the permeability of the inlet and outlet tubing and the microchannel flow distributors at the entry zone and collectors at the exit zone. Judging from the results, the aforementioned value overestimates the actual absolute permeability. That seems to contradict the statement at the end of the previous subsection; absolute permeability does not have a direct effect as it is used to reduce the analysis in dimensionless form (Eq. 8). Yet, that attribute pertains to two-phase flow in pore network conditions. Pure, fully saturated, independent Poisseuille flow at the inlet tubing of the network bias the pressure drop measurements and spoils any direct comparison between the theoretically estimated value of $f^*_{EU\infty}$, through Eq. 23, and the trend observed in the f^*_{EU} markers on the diagram in Fig. 9a. We recall here that the energy efficiency is reduced by the power dissipation of an equivalent single-phase flow.

Critical flow conditions (CFCs), corresponding to the detected energy efficiency maxima, are displayed in the diagram in Fig. 9b. These are identified by observing the maximum values of the energy efficiency in the combined rel-perm and energy efficiency diagrams in Fig. 4 and looking up values in Table A1.1. We may recall here the definition of critical flow conditions as the conditions whereby the flow rate of the NWP per unit of hydraulic power necessary to maintain the mixed flow takes maximum values. This is evaluated in an appropriately reduced form by the energy efficiency index, Eq. 17.

On the diagram in Fig. 9b, both critical flow rate ratio values, $\{r^*_i, Ca_i\}$, and mobility ratio values, $\{\lambda^*_i, Ca_i\}$, are plotted in terms of logCa. We may observe a discrepancy between the mobility ratio and flow rate ratio values at CFCs; the discrepancy is pronounced at the lower part of the Ca domain, flow rate at capillary-dominated flow regimes, while it becomes insignificant at the high-Ca domain, where bulk viscosity prevails, and the effect of menisci is practically negligible. The observed discrepancy is attributed to the procedure for detecting the CFCs and the associated mobility and flow rate ratio values. From energy efficiency values calculated on a mobility ratio basis (refer to Eq. 17), the maximum per constant-Ca experiment, $f^*_{EU}|_{Ca}$, is detected by referring to Column 13, Table A1.1, and the corresponding flow rate ratio value, $r^*|_{Ca}$, is traced by looking up in Column 5, Table A1.1.

Returning to the diagram in Fig. 9b, the detected CFCs show a tendency to line up on an S-shaped curve. This tendency is a little bit fuzzy in the low-Ca regime. To overcome this fuzziness, we have defined the log-average values of $\{r^*, \lambda^*\}$ per CFC, log$\hat{r}^*$, calculated as

$$\log\hat{r}^* = \frac{\log r^*}{2} + \frac{\log\lambda^*}{2} \;\Rightarrow\; \hat{r}^* = \sqrt{r^*\lambda^*}. \tag{24}$$

These values are also marked on the CFC diagram, Fig. 9b, by the upright cross markers (+). Now, the trend in the CFCs markers fits better to an S-shape curve.

In the same diagram, the dashed red horizontal line indicates the nominal value of the critical flow rate ratio for pure viscous flow conditions (as $Ca\to\infty$). Given the viscosity ratio value of the examined NWP/WP system, $\kappa = 0.736$, the theoretical (nominal) value of the critical flow rate ratio for pure viscous flow conditions is estimated to be (Valavanides, 2018b)

$$r^*_\infty = 1/\sqrt{\kappa} = 1/\sqrt{0.736} = 1.1656 \tag{25}$$
$$\Rightarrow\; \log r^*_\infty = 0.06656\,.$$

We may fit the available $\{\hat{r}^*_i, Ca_i\}$ points by the S-curve expression:

$$\log\hat{r}^* = -0.33\times\tanh[3.0\times(\log Ca + 5.13)] + 0.35. \tag{26}$$

The actual value attained within the lower part of the S-shape form, pertaining to larger Ca-values, indicates an asymptotic trend, from the Eq. 26, as $Ca\to\infty$, $\log\hat{r}^*_\infty \to 0.02$, flow rate, a value that is remarkably close to the theoretically predicted value, r^*_∞, from Eq. 25. That is, at viscous flows (high-Ca regimes), albeit the maximum energy efficiency does not closely match the theoretically predicted value, $f^*_{EU\infty}$, of the "ceiling of efficiency," Eq. 23, the corresponding CFCs are more accurately located when compared to the theoretically predicted CFCs, r^*_∞, through Eq. 25. The former observation is because the estimation of the energy efficiency is spoiled by the inlet microchanneling, as already discussed in the paragraph following Eq. 23. Yet, as this spoiling is uniform, it does not have a direct impact on the detection of the maximum values, hence the detection of the CFCs. Moving on to the low-Ca regime (capillary flows), the observed fuzziness in locating the CFCs is attributed to significant capillary end effects. Either the small size/short

length of the microfluidic network did not provide the flow the opportunity to attain a fully developed structure, or the effects of capillarity cannot be suppressed by viscosity. As a consequence, the structure of the (capillary) flow may be trapped in only a subdomain of the ensemble of all physically admissible interstitial flow configurations. Shifting the flow configuration from one subdomain to another subdomain requires some kind of triggering instigated by perturbations in the local hydraulic energy input.

Overall, both diagrams in Fig. 9 are similar to those furnished by Valavanides (2018b, Figs. 6 and 7) on the expected universal layout of the energy efficiency curve and locus of CFCs. The same applies also to diagrams produced in the course of a recent—conceptually similar—study on a set of SCAL measurements of relative permeabilities on a natural core and across a broad domain of flow conditions, *Ca* and *r* (Valavanides et al., 2020).

Applications in SCAL and More

The proposed flow-rate-dependent relative permeability scaling model, together with the energy efficiency and critical flow conditions, has potential applications in core analysis and reservoir engineering.

The main context is in addressing the problem of two-fluid flow in pore networks on the basis of established fully developed flow conditions or the presence of capillary end effects. Fully developed flow is not a condition always attained in SCAL measurements, as the evolution of the interstitial flow depends on the structure of the pore network, the wettability of the fluid system, and the flow conditions (the intensity of the co-injection). In general, end effects are pronounced when capillarity-associated phenomena are not suppressed by viscous resistances. The proposed methodology can be applied in SCAL, but the results will be conditionally biased by end effects. Yet, implementing a few checks, some of these simple, e.g., comparing the imposed flow rate ratio and measured mobility ratio, and some a bit more complicated, e.g., energy efficiency analysis in terms of flow conditions, we may detect the presence or even assess the extent of end effects.

In the following, we present an indicative list of potential applications in core analysis. We confine the list in steady-state co-injections in core analysis lab measurements.

By testing the consistency of the equality between the externally imposed flow rate ratios, , and the mobility ratio values, λ, calculated from the rel-perms in a set of SCAL measurements, we may assess the extent of capillary end effects in the examined flows. That is especially important in addressing viscous capillary or capillary flow conditions.

Revealing the energy efficiency and the locus of CFC can be used in characterizing the flow system in compliance with the normative methodology proposed in Valavanides (2018b). For example, in our study, we may observe two *Ca* values corresponding to the two bends of the S-curves in the diagrams in Fig. 9, whereby the flow character changes from capillary for $\log Ca < -5.5$ to mixed capillary viscous for $-5.5 < \log Ca < -4.5$, and then to viscous for $-4.5 < \log Ca$. We may, therefore, extract a rough/coarse—albeit factual—image of the interstitial behavior/response of the two-fluid and core system. That, of course, comes at the extra cost of extensive measurements at various flow conditions. Yet, if we succeed in following the path of critical flow conditions, the number of measurements is reduced, uncertainties associated with measurement errors are minimized, and specificity/confidence is maximized (see discussion in Valavanides et al., 2016, Fig. 3). In other words, tracking the SCAL measurements along the CFCs path increases the effectiveness of the lab analysis by providing more accurate/unbiased information per unit cost.

Please note that the measurements are conventional over pressure and volumetric fluxes referenced outside the pore network or natural core, and no sophisticated technology is needed to implement the proposed methodology.

Moreover, the same external (ex-core) measurements are used to extract the structure of the IDCP curve, which is essentially the backbone of the description of the two-fluid and core system. The form of the IDCP curve provides valuable information in assessing the extent of end effects and in deciphering the structure and the characteristics of the interstitial flow structure.

We have seen that capability in the current study and also in a recent one (Valavanides et al., 2020), whereby the effective IDCP functional form has been recovered by fitting the ex-core measurements. Yet, the missing part(s) of the puzzle is evaluating the extent/severity of end effects and/or being able to cope with end effects in unbiasing the ex-core measurements to get a concise and accurate (trustworthy) relative permeability map.

Another interesting application of the proposed approach is in revealing the structure of the interstitial flow. A convincing paradigm on how the IDCP curve may be used as a forensic tool in revealing the structure of the interstitial flow is the systematic SCAL study performed on a core of natural Clasach sandstone (Valavanides et al., 2020). An analysis of the measured relative permeabilities, similar to that described in "Reveal of the Relative Permeability Scaling Incorporating Flow Rate Dependency," revealed a sharply decreasing intrinsic dynamic capillary pressure function,

$A(\log Ca)$, over moderate- to high-Ca flow conditions. That seemed to be contradicting the smooth, asymptotic transition to zero ($\log A \rightarrow 0$) depicted in Fig. 8. The sharp decrease of A at moderate-/high-Ca flow conditions was an indication of a sharp reduction of capillary resistances. The particular structure of the IDCP curve revealed the onset of emulsification at high-Ca flow rates, an intrinsic flow characteristic, from simple ex-core measurements. The paradigm indicates the forensic capabilities of the IDCP curve.

In the current study, the trend in the revealed IDCP function, depicted in Fig. 8, is consistent with video observations of the interstitial flow structure, comprising a mixture of connected WP and intermittent flow of disconnected fluidic elements of the NWP separated from the WP through capillary menisci remaining in contact to the pore walls – no emulsification observed.

A follow-up study would be to investigate the stochastic spatial structure of disconnected fluidic elements of the NWP for different flow conditions in terms of the marginal distribution, with emphasis on intermittent flow and any long-range dependence in large spatial and/or temporal scales. The analysis will eventually correlate the flow structure with end effects and provide a normative measure to evaluate the predominance of end effects.

In addition, the generalized specific characteristic invariants pertaining to the two-fluid and pore network flow system, flow rate, the locus of CFCs, the locus of crossover relative permeability conditions, as well as the IDCP curve, can be used as flow system identities and that could be a strong tool in developing flow system- or rock-typing methodologies and techniques.

In the reservoir engineering domain, the ability to handle a functional form of the relative permeabilities, accounting for true-to-mechanism flow rate dependency, may improve the specificity of the field-scale simulator or increase the efficiency of machine-learning interventions. The energy-efficiency-based analysis can be a powerful tool in assessing the operational efficiency of enhanced oil recovery or CO_2 sequestration interventions, extending the energy transition timelines of such energy-intensive activities.

CONCLUSIONS

We have assessed/validated the specificity and applicability of a new flow-dependent relative permeability scaling law that integrates capillarity effects. Flow dependency is associated with the flow intensities of the NWP and WP or, equivalently, to the capillary number of the WP, Ca, and the NWP/WP flow rate ratio, r. The proposed scaling is built around the IDCP function, describing the intensity of capillary effects in terms of the flow conditions, namely the capillary number. The validation was based on a set of 12 experiments of steady-state two-phase flow through a PDMS microfluidic pore network. Each experiment was run at constant Ca for the WP for a variety of volumetric flux ratio values. The experiments covered different flow conditions, spanning across four orders of magnitude in Ca and three orders of magnitude in r, over an almost rectangular domain in $Ca \times r$. The system of fluids had an NWP/WP viscosity ratio of ~0.7 and showed intermediate wettability against the PDMS network matrix.

The results suggest that it is possible to derive and implement universal, true-to-mechanism functions describing correctly the flow dependency of relative permeabilities. The critical step here is to infer and then data fit an appropriate form of the IDCP function, $A(\log Ca)$. The IDCP function is associated with the complex rheologic character of the NWP/WP/PM system manifesting itself across the entire Ca domain.

By implementing the proposed analysis, it was possible to gain a consistent and well-structured view of the process over the domain of examined flow conditions. The calculated values of reduced quantities (reduced pressure gradient, IDCP function, energy efficiency, and locus of critical flow conditions) show a consistent dependency on flow conditions and NWP/WP/PM system properties. These can be used to reveal the interstitial flow mechanisms as well as provide an identity of the examined system.

Reviewing the present work, we may conclude:

(a) Implementation of the proposed scaling is possible using rather simple and well-known interventions typical of regular core analysis protocols; moreover, it was possible to rely on superficial measurements only, i.e., flow rates of the two phases, pressure drop across the core length, interfacial tension, and absolute permeability. We have not considered *a priori* equal pressure gradients across the pore network. Instead, we have based our post-analysis on considering pressure drops for each phase. It turned out that equality of pressure gradients is a testable hypothesis, and capillary end effects are—to a certain degree—detectable.

(b) The existence, uniqueness, and form of the locus of CFCs, $r^*(Ca)$, was confirmed. The S-shape type, confined between two asymptotic limits, as proposed in Valavanides (2018b), is also confirmed. Differences

between nominal, expected, and actual measured values are also justified.

(c) By implementing the proposed scaling and considering the underlying mechanisms of the interstitial flows, we can explain the flow behavior by referring to the macroscopic measurements. That was possible by examining the structure of the WP relative permeability, k_{rw}, and of the IDCP function, $A(\log Ca)$, without any need to examine the flow at the pore scale using sophisticated equipment. Therefore, the proposed scaling could potentially serve as an additional tool for quality assessment (or forensics) in SCAL measurements.

Based on the results of this preliminary assessment, it would make sense to consider designing and deploying a systematic laboratory study to investigate and reveal the effects of wettability, pore network structure, core size, etc., on the form of IDCP curve, $A(\log Ca)$. The scope would be to further examine if the proposed methodology can be implemented to improve SCAL and dynamic rock-typing protocols and also to develop more robust and accurate macroscopic scale models.

ACKNOWLEDGMENTS

M.S. Valavanides would like to thank:

1. The German Academic Exchange Service (DAAD - 5752335 Research Stays for University Academics and Scientists, 2021)
2. The Society of Petrophysicists and Well Log Analysts (SPWLA Foundation Board, 2021 award)

N. Karadimitriou and H. Steeb would like to thank:

1. The Deutsche Forschungsgemeinschaft (DFG) for supporting this work by funding EXC2075-390740016 under Germany's Excellence Strategy
2. The DFG for supporting this work by funding the Sonderforschungsbereich (SFB) 1313 Project 327154368

The data sets for boundary phase pressures and the corresponding fluxes are available at the Data Repository of the University of Stuttgart (DaRUS), DOI: 10.18419/darus-2816.

NOMENCLATURE

Abbreviations

CFC = critical flow conditions
DaRUS = Data Repository of the University of Stuttgart
IDCP = intrinsic dynamic capillary pressure
NWP = nonwetting phase
PDMS = Poly-Di-Methyl-Siloxane
PM = porous medium
REV = representative elementary volume
SCAL = special core analysis laboratory
WP = wetting phase

Symbols

Latin

A = kernel function, 1
$\tilde{A}$ = cross-sectional area of the pore network perpendicular to the flow, m^2
Ca = capillary number (conventional definition), 1
f_{EU} = energy efficiency, 1
k_{rn} = relative permeability of nonwetting phase, 1
k_{rw} = relative permeability of wetting phase, 1
$\tilde{U}$ = superficial velocity, m/s
$\tilde{k}$ = absolute permeability, m^2
$\tilde{p}$, $\tilde{P}$ = pressure, N/m^2
$\tilde{q}$ = volumetric flow rate, m^3/s
x = reduced pressure gradient, 1

Greek

$\tilde{\gamma}_{nw}$ = interphasial tension, N/m
Δ = difference
(θ_A, θ_R) = dynamic advancing and receding contact angles
θ = dynamic contact angle (meniscus to pore wall), 1
κ = (nonwetting/wetting) viscosity ratio, 1
λ = (nonwetting/wetting) mobility ratio, 1
$\tilde{\mu}$ = dynamic viscosity, Pa s

REFERENCES

Armstrong, R.T., McClure, J.E., Berrill, M.A., Rücker, M., Schlüter, S., and Berg, S., 2016, Beyond Darcy's Law: The Role of Phase Topology and Ganglion Dynamics for Two-Fluid Flow, *Physical Review E*, **94**(4), 043113. DOI: 10.1103/PhysRevE.94.043113.

Aursjø, O., Erpelding, M., Tallakstad, K.T., Flekkøy, E.G., Hansen, A., and Maloy, K.J., 2014, Film Flow Dominated Simultaneous Flow of Two Viscous Incompressible Fluids Through a Porous Medium, *Frontiers in Physics*, **2**(63), 1–9. DOI: 10.3389/fphy.2014.00063.

Bear, J., 2018, *Modeling Phenomena of Flow and Transport in Porous Media*, *Theory and Applications of Transport in Porous Media*, Springer. ISBN: 978-3-319-72826-1 (eBook). DOI: 10.1007/978-3-319-72826-1.

Datta, S.S., Ramakrishnan, T.S., and Weitz, D.A., 2014, Mobilization of a Trapped Non-Wetting Fluid From a Three Dimensional Porous Medium, *Physics of Fluids*, **26**(2), 022002. DOI: 10.1063/1.4866641.

Georgiadis, A., Berg, S., Makurat, A., Maitland, G., and Ott, H., 2013, Pore-Scale Micro-Computed-Tomography Imaging: Nonwetting-Phase Cluster-Size Distribution During Drainage and Imbibition, *Physical Review E*, **88**(3–1), 033002, 1–9. DOI: 10.1103/PhysRevE.88.033002.

Gervais, T., El-Ali, J., Gunther, A., and Jensen, K.F., 2006, Flow-Induced Deformation of Shallow Microfluidic Channels, *Lab on a Chip*, **6**(4), 500–507. DOI: 10.1039/b513524a.

Guillen, V.R., Carvalho, M.S., and Alvarado, V., 2012, Pore Scale and Macroscopic Displacement Mechanisms in Emulsion Flooding, *Transport in Porous Media*, **94**, 197–206. DOI: 10.1007/s11242-012-9997-9.

Karadimitriou, N.K., Musterd, M., Kleingeld, P.J., Kreutzer, M.T., Hassanizadeh, S.M., and Joekar-Niasar, V., 2013, On the Fabrication of PDMS Micromodels by Rapid Prototyping, and Their Use in Two-Phase Flow Studies, *Water Resources Research*, **49**(4), 2056–2067. DOI: 10.1002/wrcr.20196.

Oughanem, R., Youssef, S., Bauer, D., Peysson, Y., Maire, E., and Vizika, O., 2015, A Multi-Scale Investigation of Pore Structure Impact on the Mobilization of Trapped Oil by Surfactant Injection, *Transport in Porous Media*, **109**, 673-692. DOI: 10.1007/s11242-015-0542-5.

Rücker, M., Georgiadis, A., Armstrong, R.T., Ott, H., Brussee, N., van der Linde, H., Simon, L., Enzmann, F., Kersten, M., and Berg, S., 2021, The Origin of Non-thermal Fluctuations in Multiphase Flow in Porous Media., *Frontiers in Water*, **3**(671399), 1–25. DOI: 10.3389/frwa.2021.671399.

Sinha, S., Bender, A.T., Danczyk, M., Keepseagle, K., Prather, C.A., Bray, J.M., Thrane, L.W., Seymour, J.D., Codd, S.I., and Hansen, A., 2017, Effective Rheology of Two-Phase Flow in Three-Dimensional Porous Media: Experiment and Simulation, *Transport in Porous Media*, **119**, 77–94. DOI: 10.1007/s11242-017-0874-4.

Tallakstad, K.T., Knudsen, H.A., Ramstad, T., Løvoll, G., Maløy, K.J., Toussaint, R., and Flekkøy, E.G., 2009, Steady-State Two-Phase Flow in Porous Media: Statistics and Transport Properties, *Physical Review Letters*, **102**(7), 074502, 1–4. DOI: 10.1103/PhysRevLett.102.074502.

Tsakiroglou, C.D., Avraam, D.G., and Payatakes, A.C., 2007, Transient and Steady-State Relative Permeabilities From Two-Phase Flow Experiments in Planar Pore Networks, *Advances in Water Resources*, **30**(9), 1981–1992. DOI: 10.1016/j.advwatres.2007.04.002.

Tsakiroglou, C.D., Aggelopoulos, C.A., Terzi, K., Avraam, D.G., and Valavanides, M.S., 2015, Steady-State Two-Phase Relative Permeability Functions of Porous Media: A Revisit, *International Journal of Multiphase Flow*, **73**, 34–42. DOI: 10.1016/j.ijmultiphaseflow.2015.03.001.

Valavanides, M.S., Constantinides, G.N., and Payatakes, A.C., 1998, Mechanistic Model of Steady-State Two-Phase Flow in Porous Media Based on Ganglion Dynamics, *Transport in Porous Media*, **30**, 267–299. DOI: 10.1023/A:1006558121674.

Valavanides, M.S., Totaj, E., and Tsokopoulos, M., 2016, Energy Efficiency Characteristics in Steady-State Relative Permeability Diagrams of Two-Phase Flow in Porous Media, *Journal of Petroleum Science and Engineering*, **147**, 181–201. DOI: 10.1016/j.petrol.2016.04.039.

Valavanides, M.S., 2018a, Oil Fragmentation, Interfacial Surface Transport and Flow Structure Maps for Two-Phase Flow in Model Pore Networks, Predictions Based on Extensive, DeProF Model Simulations, *Oil & Gas Science and Technology – Revue d'IFP Energies Nouvelles*, **73**(6), 1–36. DOI: 10.2516/ogst/2017033.

Valavanides, M.S., 2018b, Review of Steady-State Two-Phase Flow in Porous Media: Independent Variables, Universal Energy Efficiency Map, Critical Flow Conditions, Effective Characterization of Flow and Pore Network, *Transport in Porous Media*, **123**(1), 45–99. DOI: 10.1007/s11242-018-1026-1.

Valavanides, M.S., 2018c, Universal, Flow Dependent Relative Permeability Scaling for Steady-State Two-Phase Flows in Porous Media, *International Symposium of the Society of Core Analysts*, SCA2018-060, Trondheim, Norway, 27–30 August. URL: https://www.jgmaas.com/SCA/2018/SCA2018-060.pdf. Accessed August 30, 2023.

Valavanides, M.S., Mascle, M., Youssef, S., and Vizika, O., 2020, Steady-State Two-Phase Flow in Porous Media: Laboratory Validation of Flow Dependent Relative Permeability Scaling, *E3S Web of Conferences*, **146**(03002), The 2019 International Symposium of the Society of Core Analysts. DOI: 10.1051/e3sconf/202014603002.

Valavanides, M.S., 2023, Flowrate Dependency of Steady State Two-Phase Flows in Pore Networks: Universal, Relative Permeability Scaling Function and System Characteristic Invariants, *Transport in Porous Media*, accepted for publication, in press. DOI: 10.1007/s11242-023-02012-5.

Xia, Y., and Whitesides, G.M., 1998, Soft Lithography, *Annual Review of Materials Science*, **28**, 153–184. DOI: 10.1146/annurev.matsci.28.1.153.

APPENDIX 1

Table A1.1—The Raw Data Values Measured or Calculated in the Course of the Present Study*

1	2	3	4	5	6	7	8	9	10	11	12	13
$\tilde{q}_n$	$\tilde{q}_w$	$\tilde{U}_w$	Ca	r	$\langle\tilde{P}_n\rangle$	$\langle\tilde{P}_w\rangle$	$\langle\frac{d\tilde{P}_n}{d\tilde{z}}\rangle$	$\langle\frac{d\tilde{P}_w}{d\tilde{z}}\rangle$	k_{rn}	k_{rw}	λ	f_{EU}
		Eq. 7	Eq. 9	Eq. 10			Eq. 15		Eq. 16	Eq. 16	Eq. ?	Eq. 17
[ml/min]	[ml/min]	[m/s]	[-]	[-]	[mbar]	[mbar]	[N/m]	[N/m]	[-]	[-]	[-]	[-]
0.00005	**0.0005**	1.94	**4.789**	0.10	3.047	23.093	1.523E+04	1.155E+05	0.0016	0.0028	0.758	0.0012
0.0001		×10^{-5}	**×10^{-7}**	0.20	3.885	26.663	1.942E+04	1.333E+05	0.0025	0.0024	1.373	0.0014
0.0002				0.40	9.456	26.097	4.728E+04	1.305E+05	0.0020	0.0025	1.104	0.0013
0.0003				0.60	7.618	19.317	3.809E+04	9.658E+04	0.0038	0.0034	1.521	0.0020
0.0004				0.80	10.636	24.927	5.318E+04	1.246E+05	0.0036	0.0026	1.875	0.0017
0.0005				1.00	12.301	24.752	6.151E+04	1.238E+05	0.0039	0.0026	2.012	0.0018
0.0010				2.00	8.850	20.592	4.425E+04	1.030E+05	0.0108	0.0032	4.654	0.0026
0.0020				4.00	10.926	24.860	5.463E+04	1.243E+05	0.0175	0.0026	9.101	0.0024
0.0025				5.00	27.167	37.382	1.358E+05	1.869E+05	0.0088	0.0017	6.880	0.0015
0.0050				10.00	26.048	35.363	1.302E+05	1.768E+05	0.0184	0.0018	13.576	0.0017
0.0075				15.00	32.429	52.755	1.621E+05	2.638E+05	0.0221	0.0012	24.402	0.0012
0.0100				20.00	36.484	47.253	1.824E+05	2.363E+05	0.0262	0.0014	25.903	0.0013
0.0150				30.00	52.456	52.607	2.623E+05	2.630E+05	0.0274	0.0012	30.086	0.0012
0.0200				40.00	49.739	63.906	2.487E+05	3.195E+05	0.0385	0.0010	51.394	0.0010
0.00010	**0.001**	3.876	**9.577**	0.10	10.194	11.882	5.097E+04	5.941E+04	0.0009	0.0109	0.117	0.0011
0.00025		×10^{-5}	**×10^{-7}**	0.25	22.375	31.114	1.119E+05	1.556E+05	0.0011	0.0042	0.348	0.0011
0.00050				0.50	22.944	30.879	1.147E+05	1.544E+05	0.0021	0.0042	0.673	0.0017
0.00075				0.75	26.508	34.476	1.325E+05	1.724E+05	0.0027	0.0038	0.975	0.0019
0.001				1.00	34.325	35.340	1.716E+05	1.767E+05	0.0028	0.0037	1.030	0.0019
0.002				2.00	36.810	44.825	1.840E+05	2.241E+05	0.0052	0.0029	2.436	0.0021
0.002				2.00	33.157	41.295	1.658E+05	2.065E+05	0.0058	0.0031	2.491	0.0022
0.004				4.00	38.910	49.098	1.946E+05	2.455E+05	0.0098	0.0026	5.047	0.0022
0.006				6.00	62.162	65.911	3.108E+05	3.296E+05	0.0092	0.0020	6.362	0.0017
0.008				8.00	34.605	42.031	1.730E+05	2.102E+05	0.0221	0.0031	9.717	0.0028
0.008				8.00	35.198	39.990	1.760E+05	2.000E+05	0.0218	0.0033	9.089	0.0029
0.010				10.00	39.320	42.123	1.966E+05	2.106E+05	0.0243	0.0031	10.713	0.0028
0.015				15.00	53.364	55.457	2.668E+05	2.773E+05	0.0269	0.0023	15.588	0.0022
0.0005	**0.005**	1.938	**4.789**	0.10	20.841	26.362	1.042E+05	1.318E+05	0.0023	0.0247	0.126	0.0028
0.0010		×10^{-4}	**×10^{-6}**	0.20	26.664	47.191	1.333E+05	2.360E+05	0.0036	0.0138	0.354	0.0036
0.0020				0.40	41.579	67.162	2.079E+05	3.358E+05	0.0046	0.0097	0.646	0.0038
0.0040				0.80	32.285	50.396	1.614E+05	2.520E+05	0.0119	0.0129	1.249	0.0072
0.0050				1.00	37.211	50.223	1.861E+05	2.511E+05	0.0129	0.0129	1.350	0.0074
0.0100				2.00	49.691	62.979	2.485E+05	3.149E+05	0.0193	0.0103	2.535	0.0074
0.0200				4.00	60.416	82.081	3.021E+05	4.104E+05	0.0317	0.0079	5.434	0.0067
0.0300				6.00	85.575	99.445	4.279E+05	4.972E+05	0.0336	0.0065	6.972	0.0057
0.0500				10.00	85.553	95.964	4.278E+05	4.798E+05	0.0559	0.0068	11.217	0.0062
0.0700				14.00	101.958	102.830	5.098E+05	5.142E+05	0.0657	0.0063	14.120	0.0059
0.0010	**0.015**	5.81	**1.437**	0.07	17.540	67.767	8.770E+04	3.388E+05	0.0055	0.0288	0.258	0.0059
0.0050		×10^{-4}	**×10^{-5}**	0.33	22.978	68.105	1.149E+05	3.405E+05	0.0208	0.0286	0.988	0.0142
0.0075				0.50	26.247	67.867	1.312E+05	3.393E+05	0.0273	0.0287	1.293	0.0162
0.0100				0.67	29.847	67.646	1.492E+05	3.382E+05	0.0321	0.0288	1.511	0.0174
0.0125				0.83	33.026	67.657	1.651E+05	3.383E+05	0.0362	0.0288	1.707	0.0182
0.0150				1.00	36.885	68.026	1.844E+05	3.401E+05	0.0389	0.0287	1.844	0.0186
0.0250				1.67	48.411	72.963	2.421E+05	3.648E+05	0.0494	0.0267	2.512	0.0191
0.0500				3.33	72.020	98.813	3.601E+05	4.941E+05	0.0664	0.0197	4.573	0.0162
0.0750				5.00	101.355	123.762	5.068E+05	6.188E+05	0.0708	0.0158	6.105	0.0135
0.1000				6.67	118.992	135.779	5.950E+05	6.789E+05	0.0804	0.0144	7.607	0.0127
0.1250				8.33	135.794	141.265	6.790E+05	7.063E+05	0.0881	0.0138	8.669	0.0124
0.1500				10.00	153.254	147.290	7.663E+05	7.365E+05	0.0937	0.0132	9.611	0.0120
0.2000				13.33	187.359	174.614	9.368E+05	8.731E+05	0.1022	0.0112	12.426	0.0103
0.0010	**0.02**	7.751	**1.915**	0.05	13.449	32.642	6.724E+04	1.632E+05	0.0071	0.0797	0.121	0.0086
0.0025		9	**×10^{-5}**	0.13	16.622	34.057	8.311E+04	1.703E+05	0.0144	0.0764	0.256	0.0156
0.0050		×10^{-4}		0.25	20.501	34.232	1.025E+05	1.712E+05	0.0233	0.0760	0.417	0.0224
0.0075				0.38	24.337	33.551	1.217E+05	1.678E+05	0.0295	0.0775	0.517	0.0264

1	2	3	4	5	6	7	8	9	10	11	12	13
$\tilde{q}_n$	$\tilde{q}_w$	$\tilde{U}_w$	Ca	r	$\langle\tilde{P}_n\rangle$	$\langle\tilde{P}_w\rangle$	$\langle\frac{d\tilde{P}_n}{d\tilde{z}}\rangle$	$\langle\frac{d\tilde{P}_w}{d\tilde{z}}\rangle$	k_{rn}	k_{rw}	λ	f_{EU}
		Eq. 7	Eq. 9	Eq. 10			Eq. 15		Eq. 16	Eq. 16	Eq. ?	Eq. 17
[ml/min]	[ml/min]	[m/s]	[-]	[-]	[mbar]	[mbar]	[N/m]	[N/m]	[-]	[-]	[-]	[-]
0.0100				0.50	24.878	33.527	1.244E+05	1.676E+05	0.0385	0.0776	0.674	0.0312
0.0125				0.63	30.923	34.291	1.546E+05	1.715E+05	0.0387	0.0759	0.693	0.0311
0.0150				0.75	36.769	34.296	1.838E+05	1.715E+05	0.0390	0.0758	0.700	0.0312
0.0175				0.88	38.435	35.197	1.922E+05	1.760E+05	0.0436	0.0739	0.801	0.0329
0.0200				1.00	43.743	57.008	2.187E+05	2.850E+05	0.0438	0.0456	1.303	0.0258
0.0300				1.50	59.283	58.514	2.964E+05	2.926E+05	0.0484	0.0445	1.481	0.0265
0.0500				2.50	82.338	74.893	4.117E+05	3.745E+05	0.0581	0.0347	2.274	0.0241
0.0750				3.75	107.558	90.981	5.378E+05	4.549E+05	0.0667	0.0286	3.172	0.0217
0.1000				5.00	125.317	101.947	6.266E+05	5.097E+05	0.0764	0.0255	4.068	0.0205
0.1500				7.50	156.651	133.695	7.833E+05	6.685E+05	0.0916	0.0195	6.401	0.0168
0.2000				10.00	197.028	156.018	9.851E+05	7.801E+05	0.0971	0.0167	7.919	0.0148
0.3000				15.00	256.103	198.126	1.281E+06	9.906E+05	0.1121	0.0131	11.604	0.0121
0.001	**0.025**	9.69	**2.394**	0.04	21.731	36.714	1.087E+05	1.836E+05	0.0044	0.0886	0.068	0.0056
0.005		$\times10^{-4}$	$\times10^{-5}$	0.20	30.278	54.930	1.514E+05	2.746E+05	0.0158	0.0592	0.363	0.0158
0.010				0.40	43.517	55.302	2.176E+05	2.765E+05	0.0220	0.0588	0.508	0.0198
0.020				0.80	45.137	63.254	2.257E+05	3.163E+05	0.0424	0.0514	1.121	0.0272
0.025				1.00	52.250	63.160	2.613E+05	3.158E+05	0.0458	0.0515	1.209	0.0282
0.040				1.60	71.690	68.000	3.585E+05	3.400E+05	0.0534	0.0478	1.518	0.0288
0.080				3.20	116.879	109.647	5.844E+05	5.482E+05	0.0655	0.0297	3.002	0.0222
0.120				4.80	144.029	124.038	7.201E+05	6.202E+05	0.0797	0.0262	4.134	0.0211
0.200				8.00	199.532	167.792	9.977E+05	8.390E+05	0.0959	0.0194	6.727	0.0169
0.250				10.00	225.260	184.310	1.126E+06	9.216E+05	0.1062	0.0176	8.182	0.0157
0.001	**0.04**	1.55	**3.831**	0.03	28.796	60.743	1.440E+05	3.037E+05	0.0033	0.0856	0.053	0.0043
0.004		$\times10^{-3}$	$\times10^{-5}$	0.10	21.578	58.164	1.079E+05	2.908E+05	0.0177	0.0894	0.270	0.0190
0.008				0.20	33.036	60.500	1.652E+05	3.025E+05	0.0232	0.0860	0.366	0.0231
0.012				0.30	44.289	61.759	2.214E+05	3.088E+05	0.0259	0.0842	0.418	0.0248
0.020				0.50	46.170	67.162	2.309E+05	3.358E+05	0.0415	0.0775	0.727	0.0326
0.040				1.00	63.346	74.746	3.167E+05	3.737E+05	0.0604	0.0696	1.180	0.0377
0.080				2.00	86.214	99.599	4.311E+05	4.980E+05	0.0888	0.0522	2.311	0.0365
0.120				3.00	107.158	109.802	5.358E+05	5.490E+05	0.1072	0.0474	3.074	0.0358
0.200				5.00	155.556	141.517	7.778E+05	7.076E+05	0.1230	0.0368	4.549	0.0301
0.400				10.00	259.205	204.070	1.296E+06	1.020E+06	0.1477	0.0255	7.873	0.0226
0.001	**0.04**	1.55	**3.831**	0.03	12.688	39.154	6.344E+04	1.958E+05	0.0075	0.1329	0.077	0.0095
0.005		$\times10^{-3}$	$\times10^{-5}$	0.13	15.463	43.311	7.732E+04	2.166E+05	0.0309	0.1201	0.350	0.0311
0.010				0.25	27.006	43.631	1.350E+05	2.182E+05	0.0354	0.1192	0.404	0.0343
0.020				0.50	49.333	64.159	2.467E+05	3.208E+05	0.0388	0.0811	0.650	0.0320
0.030				0.75	44.473	66.749	2.224E+05	3.337E+05	0.0646	0.0779	1.126	0.0413
0.040				1.00	57.907	64.507	2.895E+05	3.225E+05	0.0661	0.0806	1.114	0.0425
0.080				2.00	87.260	90.627	4.363E+05	4.531E+05	0.0877	0.0574	2.077	0.0387
0.120				3.00	111.805	94.284	5.590E+05	4.714E+05	0.1027	0.0552	2.530	0.0395
0.200				5.00	166.953	127.819	8.348E+05	6.391E+05	0.1146	0.0407	3.828	0.0323
0.400				10.00	276.704	192.623	1.384E+06	9.631E+05	0.1383	0.0270	6.961	0.0236
0.0100	**0.05**	1.938	**4.789**	0.20	22.986	54.796	1.149E+05	2.740E+05	0.0416	0.1187	0.477	0.0383
0.0500		$\times10^{-3}$	$\times10^{-5}$	1.00	65.706	75.437	3.285E+05	3.772E+05	0.0728	0.0862	1.148	0.0461
0.1000				2.00	106.743	101.952	5.337E+05	5.098E+05	0.0897	0.0638	1.910	0.0419
0.5000				10.00	316.671	218.030	1.583E+06	1.090E+06	0.1511	0.0298	6.885	0.0260
0.4000				8.00	287.735	221.396	1.439E+06	1.107E+06	0.1330	0.0294	6.156	0.0253
0.2500				5.00	231.364	186.705	1.157E+06	9.335E+05	0.1034	0.0348	4.035	0.0279
0.0400				0.80	108.234	115.543	5.412E+05	5.777E+05	0.0354	0.0563	0.854	0.0259
0.0100				0.20	78.804	100.364	3.940E+05	5.018E+05	0.0121	0.0648	0.255	0.0132
0.0050	**0.06**	2.33	**5.746**	0.08	33.246	59.640	1.662E+05	2.982E+05	0.0144	0.1308	0.149	0.0170
0.0075		$\times10^{-3}$	$\times10^{-5}$	0.13	39.554	62.095	1.978E+05	3.105E+05	0.0181	0.1257	0.196	0.0206
0.0100				0.17	44.334	62.715	2.217E+05	3.136E+05	0.0216	0.1244	0.236	0.0237
0.020				0.33	46.817	68.094	2.341E+05	3.405E+05	0.0409	0.1146	0.485	0.0374
0.030				0.50	51.547	70.654	2.577E+05	3.533E+05	0.0557	0.1104	0.685	0.0449
0.040				0.67	66.649	70.992	3.332E+05	3.550E+05	0.0574	0.1099	0.710	0.0456
0.050				0.83	72.730	76.384	3.636E+05	3.819E+05	0.0658	0.1022	0.875	0.0477

1	2	3	4	5	6	7	8	9	10	11	12	13
$\tilde{q}_n$	$\tilde{q}_w$	$\tilde{U}_w$	Ca	r	$\langle \tilde{P}_n \rangle$	$\langle \tilde{P}_w \rangle$	$\langle \frac{d\tilde{P}_n}{d\tilde{z}} \rangle$	$\langle \frac{d\tilde{P}_w}{d\tilde{z}} \rangle$	k_{rn}	k_{rw}	λ	f_{EU}
		Eq. 7	Eq. 9	Eq. 10			Eq. 15		Eq. 16	Eq. 16	Eq. ?	Eq. 17
[ml/min]	[ml/min]	[m/s]	[-]	[-]	[mbar]	[mbar]	[N/m]	[N/m]	[-]	[-]	[-]	[-]
0.060				1.00	75.081	80.097	3.754E+05	4.005E+05	0.0765	0.0974	1.067	0.0503
0.070				1.17	88.125	82.371	4.406E+05	4.119E+05	0.0760	0.0947	1.090	0.0494
0.080				1.33	94.229	93.441	4.711E+05	4.672E+05	0.0813	0.0835	1.322	0.0476
0.090				1.50	104.022	102.916	5.201E+05	5.146E+05	0.0828	0.0758	1.484	0.0453
0.100				1.67	114.718	104.849	5.736E+05	5.242E+05	0.0834	0.0744	1.523	0.0449
0.125				2.08	128.573	108.849	6.429E+05	5.442E+05	0.0930	0.0717	1.764	0.0458
0.200				3.33	186.720	146.855	9.336E+05	7.343E+05	0.1025	0.0531	2.622	0.0385
0.300				5.00	252.413	188.964	1.262E+06	9.448E+05	0.1137	0.0413	3.743	0.0326
0.500				8.33	340.164	245.881	1.701E+06	1.229E+06	0.1407	0.0317	6.024	0.0272
0.600				10.00	379.167	265.565	1.896E+06	1.328E+06	0.1514	0.0294	7.004	0.0257
0.001	**0.08**	3.10	**7.662**	0.01	28.219	79.735	1.411E+05	3.987E+05	0.0034	0.1305	0.035	0.0045
0.005		$\times 10^{-3}$	$\times 10^{-5}$	0.06	30.831	81.044	1.542E+05	4.052E+05	0.0155	0.1284	0.164	0.0181
0.010				0.13	41.321	81.259	2.066E+05	4.063E+05	0.0232	0.1280	0.246	0.0253
0.025				0.31	50.655	87.577	2.533E+05	4.379E+05	0.0472	0.1188	0.540	0.0417
0.050				0.63	71.013	99.191	3.551E+05	4.960E+05	0.0674	0.1049	0.873	0.0489
0.080				1.00	91.684	113.404	4.584E+05	5.670E+05	0.0835	0.0918	1.237	0.0507
0.100				1.25	113.234	128.601	5.662E+05	6.430E+05	0.0845	0.0809	1.420	0.0475
0.200				2.50	191.120	179.927	9.556E+05	8.996E+05	0.1001	0.0578	2.354	0.0406
0.400				5.00	293.241	242.918	1.466E+06	1.215E+06	0.1305	0.0428	4.142	0.0345
0.800				10.00	435.924	326.819	2.180E+06	1.634E+06	0.1756	0.0318	7.497	0.0281
0.010	**0.1**	3.88	**9.577**	0.10	45.990	105.394	2.299E+05	5.270E+05	0.0208	0.1234	0.229	0.0230
0.025		$\times 10^{-3}$	$\times 10^{-5}$	0.25	62.169	106.963	3.108E+05	5.348E+05	0.0385	0.1216	0.430	0.0366
0.050				0.50	82.150	114.395	4.107E+05	5.720E+05	0.0582	0.1137	0.696	0.0467
0.075				0.75	88.776	116.020	4.439E+05	5.801E+05	0.0809	0.1121	0.980	0.0555
0.100				1.00	108.151	119.126	5.408E+05	5.956E+05	0.0885	0.1092	1.101	0.0572
0.150				1.50	143.620	144.499	7.181E+05	7.225E+05	0.1000	0.0900	1.509	0.0541
0.300				3.00	243.904	209.383	1.220E+06	1.047E+06	0.1177	0.0621	2.575	0.0447
0.500				5.00	327.528	248.211	1.638E+06	1.241E+06	0.1461	0.0524	3.789	0.0415
1.000				10.00	511.587	365.910	2.558E+06	1.830E+06	0.1871	0.0355	7.152	0.0312
0.010	**0.12**	4.65	**1.149**	0.08	50.943	104.308	2.547E+05	5.215E+05	0.0188	0.1496	0.171	0.0218
0.025		$\times 10^{-3}$	$\times 10^{-4}$	0.21	74.715	112.848	3.736E+05	5.642E+05	0.0320	0.1383	0.315	0.0331
0.050				0.42	78.529	123.548	3.926E+05	6.177E+05	0.0609	0.1263	0.656	0.0500
0.075				0.63	98.494	129.806	4.925E+05	6.490E+05	0.0729	0.1202	0.824	0.0543
0.100				0.83	117.073	136.503	5.854E+05	6.825E+05	0.0817	0.1143	0.972	0.0563
0.120				1.00	127.211	142.734	6.361E+05	7.137E+05	0.0903	0.1093	1.122	0.0578
0.150				1.25	149.711	156.809	7.486E+05	7.840E+05	0.0959	0.0995	1.309	0.0564
0.200				1.67	180.082	173.220	9.004E+05	8.661E+05	0.1063	0.0901	1.603	0.0555
0.500				4.17	342.762	270.634	1.714E+06	1.353E+06	0.1396	0.0577	3.290	0.0442
0.750				6.25	441.911	327.768	2.210E+06	1.639E+06	0.1624	0.0476	4.636	0.0392
1.000				8.33	523.742	377.316	2.619E+06	1.887E+06	0.1827	0.0414	6.004	0.0355
1.200				10.00	578.127	403.809	2.891E+06	2.019E+06	0.1986	0.0387	6.985	0.0338

*The second row on the heading refers to the equation used to calculate the values.

ABOUT THE AUTHORS

Nikolaos Karadimitriou, serves as a post-doctoral research associate at the Institute of Applied Mechanics within the Faculty of Civil and Environmental Engineering at the University of Stuttgart, Germany. He possesses extensive expertise in the design and production of artificial porous media, tailoring them to specific flow patterns, as well as fine-tuning their physical and chemical attributes. His research primarily revolves around experimental investigations into two-phase flow and transport, encompassing both fundamental scientific inquiries and application-oriented studies. Dr. Karadimitriou has established three microfluidic laboratories across different countries and academic institutions. Additionally, he boasts substantial proficiency in utilizing and advancing various microscopy techniques, including optical, fluorescence, confocal, and thermal methods. Dr. Karadimitriou took charge of organizing and coordinating the acquisition of necessary equipment and materials for the study, developing the models, conducting preliminary research, overseeing the study's execution, collecting raw data, and contributed to the writing and review of the paper.

Marios Valavanides holds the position of professor in hydraulics and porous media flow and serves as director of the Hydraulics Lab within the Department of Civil Engineering at the University of West Attica, Athens, Greece. His primary research area centers on the true-to-mechanism modeling of two-phase flow in porous media, with a particular focus on the DeProF theoretical framework, which revolves around the flow rate dependency of two-phase flow in porous media. For further information on this framework, you can visit the following link: http://users.uniwa.gr/marval/ImproDeProF.html. Prof. Valavanides played a crucial role in envisioning and deploying this ongoing study. He formulated the research protocol, assessed the raw data, and took the lead in writing the paper. He is the corresponding author.

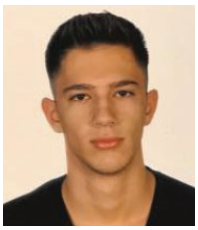

Konstantinos Mouravas is a graduate student in the Department of Civil Engineering at the University of West Attica, Athens, Greece. He became involved in the research while working on his Diploma Thesis. Mr. Mouravas played a pivotal role in carrying out various tasks of the study, such as manufacturing the models, conducting the experiments, collecting raw data, and reporting.

Holger Steeb holds the position of full professor (W3) and serves as the director of the Institute of Applied Mechanics within the Faculty of Civil and Environmental Engineering. Additionally, he is a Fellow of SC SimTech at the University of Stuttgart, Germany. Professor Steeb and his research group have conducted comprehensive examinations of the hydromechanical coupling of porous media, employing a blend of theoretical, numerical, and experimental approaches across various scales. This encompasses investigations at both the small scale, involving Direct Numerical Simulations (DNS) at the pore level, often utilizing techniques such as light- or X-ray micro-CT imaging (inclusive of in-situ hydromechanical experiments), as well as macro (continuum) scale studies. Furthermore, Professor Steeb established the "Porous Media Lab" at the University of Stuttgart, which serves as a hub for microfluidic experimental inquiries into multiphase flow. He played a critical role in reviewing the study's design, ensuring the availability of the necessary infrastructure. He surveyed the deployment of the study, provided ideas, and reviewed the results and the paper.